

# Thermochronology of sandstone-hosted secondary Fe- and Mn-oxides near Moab, Utah: Record of paleo–fluid flow along a fault

Victor H. Garcia<sup>1†</sup>, Peter W. Reiners<sup>1</sup>, David L. Shuster<sup>2,3</sup>, Bruce Idleman<sup>4</sup>, and Peter K. Zeitler<sup>4</sup>

<sup>1</sup>Department of Geosciences, University of Arizona, 1040 East 4th Street, Tucson, Arizona 85721, USA

<sup>2</sup>Department of Earth and Planetary Science, University of California–Berkeley, 307 McCone Hall, Berkeley, California 94720, USA

<sup>3</sup>Berkeley Geochronology Center, 2455 Ridge Road, Berkeley, California 94709, USA

<sup>4</sup>Department of Earth and Environmental Sciences, Lehigh University, 1 West Packer Avenue, Bethlehem, Pennsylvania 18015, USA

## ABSTRACT

Secondary Fe- and Mn-oxides are locally common near faults and fractures within sandstones of the Colorado Plateau in the form of cements, concretions, and fracture-fill material. However, little is known about how and why these oxides formed, and less is understood about when they formed. In this study, we integrated field observations, detailed scanning electron microscope and petrographic observations, and (U-Th)/He and <sup>40</sup>Ar/<sup>39</sup>Ar dating to better understand the formation of Fe- and Mn-oxides from three fault zones in Flat Iron Mesa, Utah. Most Fe- and Mn-oxide (U-Th)/He ages range from 0.50 to 3.4 Ma, which are much younger than <sup>40</sup>Ar/<sup>39</sup>Ar ages of 25–20 Ma from a previous study. Current <sup>40</sup>Ar/<sup>39</sup>Ar ages on a Mn-oxide sample from this study yielded a plateau age of 3.6 ± 0.08 Ma. <sup>4</sup>He/<sup>3</sup>He diffusion data from Fe- and Mn-oxides are consistent with the presence of multiple diffusion domains with varying He retentivity. Predicted fractional radiogenic He retention over 3.6 m.y. at near-surface temperatures for the bulk samples, with domain proportions of the diffusion experiments, is ~90% for Fe-oxide and ~45% for Mn-oxide. The multidomain behavior exhibited by the oxides and the variability observed in (U-Th)/He ages among aliquots are consistent with variable amounts of diffusive loss of He within dated aliquots. Using <sup>4</sup>He/<sup>3</sup>He data and He bulk ages, step-age plots indicate a high fractional release plateau at ca. 3.6 Ma, concordant with <sup>40</sup>Ar/<sup>39</sup>Ar dating and most of the oldest (U-Th)/He ages observed. Taken together, these results are most consistent with formation of Flat Iron Mesa Fe- and Mn-oxides near the surface (<0.5 km) at 3.6 Ma, due to hydrologic changes, fault activity, or both. Our data and

interpretations suggest that erosional exhumation rates over ~1–4 m.y. time scales may be variable in the central Colorado Plateau, possibly driven by local effects, and they are not spatially uniform over large regions.

## INTRODUCTION

Secondary Fe- and Mn-oxides are commonly found in faults, fractures, and as cement within sandstones of the Colorado Plateau (Chan et al., 2001; Beitler et al., 2003; Busigny and Dauphas, 2007; Reiners et al., 2014). Similar oxides have also been observed in many other geologic settings across the world, generally in sandstones, and as well as on Mars in the form of spherical hematite concretions (Ostwald, 1981; Laznicka, 1992; Chan et al., 2004; Squyres and Knoll, 2005; Chan et al., 2012; Leal et al., 2008; White et al., 2009; Wilson et al., 2012; Lanza et al., 2014). These secondary minerals form as the result of reactions associated with fluid flow after the associated host rock has formed. One hypothesis proposes that oxides like those in our study formed near redox reaction fronts at the interfaces between deep reduced fluids carrying dissolved Fe and Mn and near-surface oxygenated fluids (Beitler et al., 2003, 2005; Chan et al., 2005, 2007, 2006). Another proposes that they were initially precipitated as reduced minerals (i.e., siderite, rhodochrosite) and later oxidized at shallower depths (Loope et al., 2010; Kettler et al., 2011; Weber et al., 2012; Loope and Kettler, 2015). Regardless of their origins, these minerals preserve information pertaining to past fluid flow, which has the potential to constrain paleohydrology and its tectonic, geomorphic, and climatic influences over time. Our current understanding of secondary oxides is relatively primitive, at least partly because there is little agreement about when these features formed. The ability to date secondary oxides and to associate these dates with their chemical compositions and spatial patterns in the subsurface could provide

information about the timing of fluid flow, mineral precipitation, effects on modern aquifers, hydrocarbon reservoirs, and fault activity.

## Geochemical Context of Low-Temperature Secondary Fe- and Mn-Oxides

The local accumulation of Fe- and Mn-oxides is broadly mediated by changes in Eh and pH of subsurface Fe- and Mn-bearing fluids. At a given pH, Fe and Mn are more soluble at lower Eh, where they are primarily reduced species Fe<sup>2+</sup> and Mn<sup>2+</sup>, whereas their oxidized forms, Fe<sup>3+</sup>, Mn<sup>3+</sup>, and Mn<sup>4+</sup>, are highly insoluble, precipitating as oxides, hydroxides, and oxyhydroxides (which we collectively refer to here as oxides; Garrels and Christ, 1965). At intermediate Eh, basic solutions favor oxidized and therefore less soluble Fe and Mn. However, at very low pH, even oxidized Fe and Mn are soluble (e.g., acid mine drainage). The shapes of redox-pH phase equilibria boundaries for Fe and Mn in equilibrium with other major dissolved species are similar in form but do not exactly overlap. At a given pH, Mn remains reduced and soluble to higher oxidation potential than Fe. This can result in spatial fractionation of Fe and Mn precipitation along Eh gradients. Basta and Saleeb (1971) interpreted paleo-Eh gradients in brecciated zones along faults near the Egypt and Sudan border, where Fe minerals are located deeper in fault zones and Mn-oxides are closer to the surface. Similar patterns are also seen in the Pampean Ranges in Argentina, where Fe and Mn mineralization in veins precipitated at deeper and shallower levels, respectively (Leal et al., 2008; Leal, 2010).

## Geochronology and Thermochronology of Oxides

Most (U-Th)/He dating applied to secondary oxide minerals has focused on He retentivity of Fe-oxides and has shown that they can quantita-

<sup>†</sup>vhgarcia4@email.arizona.edu

tively retain He and yield reproducible formation ages that are consistent with other geological records (Wernicke and Lippolt, 1993, 1994a, 1994b; Lippolt et al., 1995; Evenson et al., 2014). Other studies, involving He diffusion experiments and (U-Th)/He dating of oxides, have shown that at least some types of goethite lose ~10% of radiogenic He at low temperatures over multimillion-year time scales (Shuster et al., 2005; Heim et al., 2006). Studies of hydrothermal hematite were able to deduce formation ages and thermal histories from polydomain behavior using (U-Th)/Ne and (U-Th)/He (Farley and Flowers, 2012). More recently, (U-Th)/Ne and (U-Th)/He thermochronology was combined to characterize the age, origin, and thermal histories of high-grade iron ore (hematite; Farley and McKeon, 2015).

(U-Th)/He dating methods, along with  $^{40}\text{Ar}/^{39}\text{Ar}$  dating techniques in some cases, have also been used in pedogenic weathering studies for both Fe- and Mn-oxides, though Mn-oxides have received much less attention in (U-Th)/He thermochronology (Shuster et al., 2005; Waltenberg, 2012; Riffel et al., 2016; Heim et al., 2006; Lippolt and Hautmann, 1995; Vasconcelos et al., 1992, 1994; Vasconcelos, 1999; Waltenberg et al., 2010; Li et al., 2002). Lippolt et al. (1995) were the first to publish He diffusion data on cryptomelane-hollandite. The Arrhenius trend from this Mn-oxide study implies an activation energy ( $E_a$ ) of 134 kJ/mol with a  $T_c$  (closure temperature) of 245 °C. Reiners et al. (2014) performed  $^4\text{He}$  diffusion experiments on Ba-rich Mn-oxide phases, and their results suggested that these phases may be able to retain large fractions of radiogenic He. One caveat is that the experiments conducted by Reiners et al. (2014) (as well as by Lippolt et al., 1995) were not done on proton-bombardment-generated  $^3\text{He}$ . Outgassing of spallation-induced  $^3\text{He}$  in minerals is used as a proxy of radiogenic  $^4\text{He}$  diffusion, which allows He diffusivity measurements to be done on samples in which the natural concentration distribution is not uniform (Shuster and Farley, 2005).

### Oxides of the Colorado Plateau

Mesozoic sandstones of the Colorado Plateau contain Fe- and Mn-oxide cement, concretions, and fracture-fill material that have precipitated as a result of previous fluid flow events. Morphologies of the oxide precipitates include spheroidal concretions (e.g., Moqui Marbles), sheets, cones, cylindrical pipes, and fracture-fill material (Chan et al., 2000; Chan et al., 2001, 2004; Beitler et al., 2003; Busigny and Dauphas, 2007; Potter and Chan, 2011; Loope et al., 2010; Reiners et al., 2014). This diversity

of occurrences has been interpreted to represent a wide variety of Fe and Mn mobilization processes involving migration of hydrocarbons (Beitler et al., 2003; Levandowski et al., 1973; Segal et al., 1986; Chan et al., 2000) and/or reduced and potentially  $\text{CO}_2$ -rich fluids (Loope et al., 2010; Wigley et al., 2012). Deducing the origins of these diverse oxides may be complicated by the possibility of multiple formation mechanisms, as well as the possibility of open-system behavior, in which oxides and groundwater may have continued to interact and chemically exchange constituents for millions of years (Reiners et al., 2014). Secondary oxide cements, concretions, and fracture-fill material may have experienced compositional changes after initial formation through time (i.e., U-Th addition, recrystallization, trace element and isotopic changes, and/or multiple episodes of precipitation).

We focus here on the Fe- and Mn-oxide cement and fracture-fill material along fault zones of the Navajo Sandstone south of Moab, Utah, in a region known as Flat Iron Mesa. Besides a recent study of hydrothermal hematite limestone in the Grand Canyon (Farley and Flowers, 2012), some of the only radioisotopic ages on secondary oxides in the Colorado Plateau come from this area. Chan et al. (2001) presented  $^{40}\text{Ar}/^{39}\text{Ar}$  age spectra of colloform cryptomelane cements between sand grains. These authors interpreted formation ages of 25–20 Ma, based on a relatively large fraction of gas with ages in this range in an otherwise complex  $^{40}\text{Ar}/^{39}\text{Ar}$  age step-heating spectrum. More recently, (U-Th)/He dating of Fe- and Mn-oxides in veins in the same region yielded ages of 3.0–2.3 Ma and 2.3–1.5 Ma, respectively (Reiners et al., 2014). Attempting to reconcile these data with the previous  $^{40}\text{Ar}/^{39}\text{Ar}$  ages, Reiners et al. (2014) proposed that these ages could be younger than the  $^{40}\text{Ar}/^{39}\text{Ar}$  ages because of postformation U addition by later fluid flow. This could be consistent with interpretations of the studies by Potter et al. (2011) and Loope et al. (2010, 2011), which inferred multiple episodes of precipitation based on concentric zonation of Fe-oxides, concretion formation prior to development of crosscutting regional fractures, or a later phase of oxide formation after a reduced Fe or Mn precursor mineral.

In this study, we used scanning electron microscope (SEM) and petrographic observations to determine a precipitation sequence, and we used both (U-Th)/He thermochronology and  $^{40}\text{Ar}/^{39}\text{Ar}$  geochronology to date secondary oxides from three nearby fault zones in the Navajo Sandstone at Flat Iron Mesa to constrain past fluid flow in the region. We also used  $^4\text{He}/^3\text{He}$  diffusion experiments from both Fe- and Mn-oxides to esti-

mate He diffusion kinetics, and we used these to interpret the fractional retention of radiogenic  $^4\text{He}$  and formation ages of the secondary oxides in this region. In fracture-fill material, Fe-oxide He ages yield relatively precise ages that more closely approximate the age of formation, whereas Mn-oxide He ages show more complex age variations that likely reflect more variable He retention since formation.

### GEOLOGIC SETTING

Southeastern Utah contains widely distributed small deposits of Fe- and Mn-oxides in host rocks ranging from the Upper Triassic to Upper Jurassic, although some are also found in much younger units (Baker et al., 1952). The deposits that we focus on in this study occur as nodules, thin centimeter-scale veins, fracture-fill material, or as cementing material between sand grains and include pyrolusite, manganite, psilomelane, hollandite group minerals, hematite, and goethite (Baker et al., 1952; Chan et al., 2000; Chan et al., 2001; Reiners et al., 2014). They are exposed in shallow trenches in fault zones that were sporadically targeted for mining in the early 1900s (Baker et al., 1952). Most, if not all, of the larger deposits have been mined, and all that remain are small deposits composed of fracture-fill material and cement.

In this study, we focused on three small oxide deposits in fault zones associated with the Moab-Lisbon system of faults and grabens in an area known as Flat Iron Mesa (Fig. 1). Flat Iron Mesa is 30 km south of Moab, Utah, and is bounded by Kane Springs Canyon to the north, Hatch Watch Canyon to the west, West Coyote Canyon to the south, and Highway 191 to the east. Flat Iron Mesa lies within the Paradox Basin, which has undergone a structurally complex history of deformation and fluid flow, as summarized in many studies (Peterson, 1989; Foxford et al., 1996, 1998; Barbeau, 2003; Solum et al., 2005; Trudgill, 2011). During the Pennsylvanian, this region accumulated sequences of carbonate, organic-rich shale, and evaporite (i.e., anhydrite, halite) formations in the ancestral Paradox Basin. Passive deformation induced by later episodes of sedimentation, unloading, and dissolution has resulted in salt-related deformation since the Early Triassic up to present day (Doelling et al., 1988; Trudgill, 2011; Jochems and Pederson, 2015). Faulting has been active in the region since the Triassic due to the Laramide orogeny, extension that followed, and salt-related deformation (Foxford et al., 1996; Barbeau, 2003; Berg and Skar, 2005; Solum et al., 2010; Frery et al., 2015). Salt-related deformation includes salt walls, diapirs, development of large roll-overs, and NW-

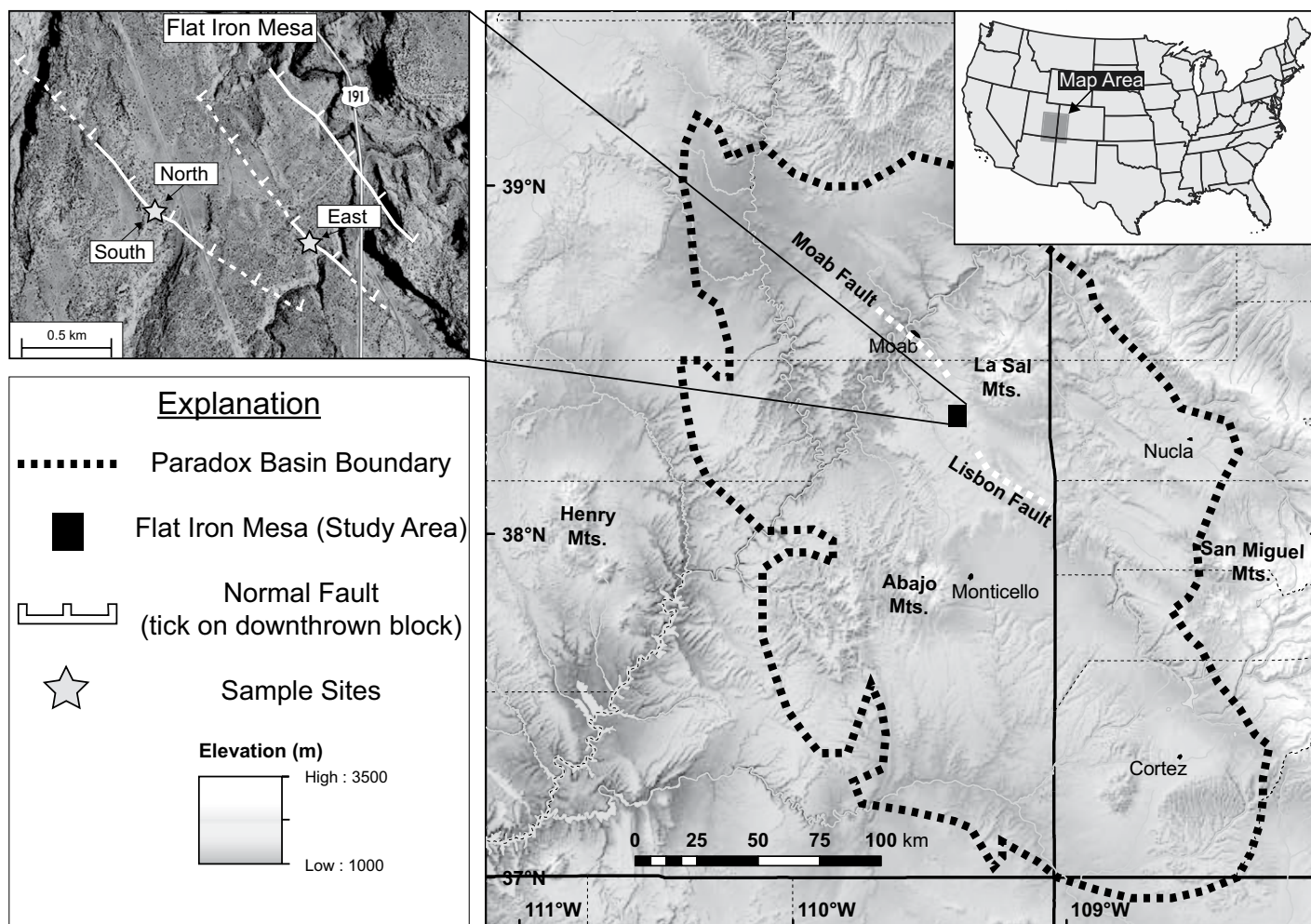


**Figure 1.** Digital elevation model (DEM) showing extent of the Paradox Basin and the locations of the Moab and Lisbon faults. The black rectangle in the DEM shows the location of Flat Iron Mesa (study area) where we collected samples within exposures of the Jurassic Navajo Sandstone off of Highway 191 south of Moab, Utah. Samples were collected from three faults known in this study as the north ( $38^{\circ}21.425'N$ ,  $109^{\circ}26.931'W$ ), south ( $38^{\circ}21.414'N$ ,  $109^{\circ}26.939'W$ ), and east faults ( $38^{\circ}21.308'N$ ,  $109^{\circ}26.234'W$ ) shown as stars. Solid and dotted white lines depict fault traces.

SE-trending folds, faults, and grabens. Locally, the major fault systems are the Moab (45 km long) and Lisbon (34 km long) faults (NW-SE-trending normal faults). The Moab fault's latest period of fault motion has been interpreted at ca. 60 Ma by K-Ar dating and  $^{40}Ar/^{39}Ar$  dating of illite-smectite, though these faults may still be active today (Foxford et al., 1996; Pevear et al., 1997; Solum et al., 2005).

The Jurassic Navajo Sandstone that hosts these secondary oxide minerals is a well-sorted, fine-grained, quartz-dominated sandstone with high porosity and permeability, and it is weakly cemented with varying amounts of quartz overgrowths, clays, carbonates, and secondary oxide cement (Chan et al., 2000; Chan et al., 2001; Beitler et al., 2003; Loope et al., 2010; Potter and Chan, 2011; Trudgill, 2011). In this location, Fe- and Mn-oxide mineralization occurred within

the Jurassic Navajo Sandstone and is observed as cement and as fracture-fill material across many faults (Chan et al., 2001; Reiners et al., 2014).

### Sample Locations

Fe- and Mn-oxide deposits occur on the surface of canyon walls and in faults that cut through canyons in Flat Iron Mesa. Samples were collected near Muleshoe Wash, west of Highway 191, where three small faults (herein referred to as the north, south, and east faults; Fig. 1) parallel both the Moab and Lisbon faults. Samples collected from the north and south faults were located several hundred meters away from the canyons in the rolling terrain. Samples from the east fault were collected from an outcrop (near an old mine shaft) a few meters away from the canyon walls of Muleshoe Wash

near Highway 191. Samples comprise two distinct observable groups at hand specimen scale: (1) Fe- and Mn-oxide cements surrounding quartz, feldspar, and other detrital sand grains, and (2) mostly pure Mn-oxide (13PRCP8U, 14VGCP10U) or pure Fe-oxide (13PRCP8L, 14VGCP10L) material precipitated as veinlets in fractures and faults. The term "oxide" is used loosely in this study to include true Fe- and Mn-oxides like hematite, pyrolusite, cryptomelane, and hollandite, as well as oxyhydroxides, such as goethite and manganite.

We collected Fe- and Mn-oxide samples from a trench at the north fault. Fe- and Mn-oxide deposits are present between fragments of sandstone and as cement between sand grains. Fracture-fill material is present as centimeter-scale veinlets throughout the trench walls (Fig. 2A). Here, Fe-oxides form botryoidal black crystals;

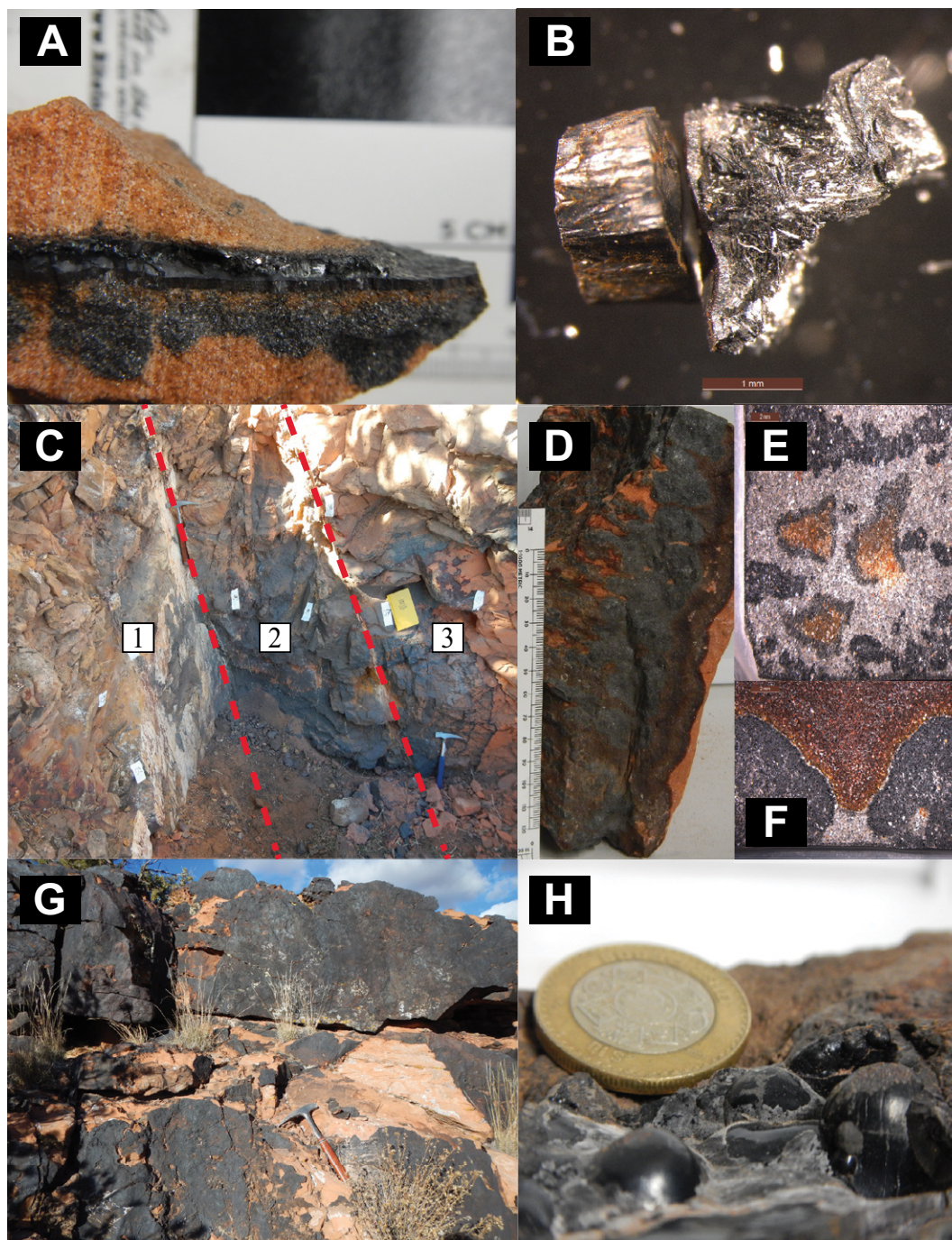


**Figure 2.** Images of representative secondary oxide samples, grains, and probe sections in this study. (A) Fracture-fill material containing Fe- and Mn-oxide; 0.5 cm thick. (B) Fe-oxide (left, black) and Mn-oxide (right, silver) aliquots used for (U-Th)/He dating. (C) Image of south fault from which Fe- and Mn-oxides were collected; samples locations are represented by white tape on outcrop. Fe-oxide is farthest away from the fractures and dominates in section 1 on image. Section 2 consists of Fe-oxide, Ba-rich Mn-oxide, and relatively pure Mn-oxide. Section 3 consists of same material of section 2 and a colloform structure (near blue hammer). (D) Colloform sample showing banding. (E) Probe section of colloform structure showing Ba-rich Mn-oxide (black) and Mn-oxide (silver). (F) Probe section of colloform structure; Fe-oxide—red, Ba-rich Mn-oxide—black, Mn-oxide—silver. (G) Image from the east fault from which samples were collected. Surface of outcrop is covered with botryoidal Fe-oxide. (H) Magnified image of botryoidal Fe-oxide.

in contrast, Mn-oxides form prismatic metallic crystals with dendritic black Mn-oxide in between prismatic crystals (Fig. 2B). Samples of fracture-fill material from the north fault were the only ones with compositions near end-member Fe- or Mn-oxide, although SEM–energy dispersive spectroscopy (EDS) examination of samples revealed noticeable differences in Ba content within Mn-oxides in the same veins.

Another mineralized fault zone, ~50 m south of the north fault, consists of two smaller faults

in which both Fe- and Mn-oxide mineralization had precipitated as dark-red Fe-oxide and metallic to black Mn-oxide cements within the Navajo Sandstone (Fig. 2C). In general, Fe-oxide cement is farthest away from the faults, whereas Mn-oxide is closer, although in some locations, Fe-oxides are found near or at faults, suggesting multiple episodes of precipitation. All (U-Th)/He data from the south fault come from Fe- and Mn-oxide cement samples. These cements occur as microscale veins to colloform

cement banding that suggest fluids emanated from the faults. This is observed in the meter-scale colloform structures observed in Figure 2C. We collected a sample from the colloform structure similar to a sample of Chan et al. (2001). This sample showed irregular curved bands of centimeter-scale digitate structures with concentric zonation in the abundance and compositions of cement as shown in Figures 2D and 2E. Parts of the cores of these structures are weakly cemented, with a transition toward the

rims to Ba-rich Mn-oxide (likely hollandite), near-end-member Mn-oxide (likely pyrolusite), and Fe-oxide cement (likely goethite). Figure 2F shows the edge of a colloform structure (mushroom shaped), where the Fe- and Mn-oxide contact is clearly seen. SEM imaging confirmed that the silver-colored material is near-end-member Mn-oxide, whereas the duller black cement is Ba-rich Mn-oxide.

The east fault is ~1 km southeast of both the north and south faults, cutting Muleshoe Wash and continuing across the highway. Samples collected from this location contain both Fe-oxide cement and botryoidal crystals from fracture surfaces. Mn-oxide fracture-fill material was not found in this area, but some does occur as cement material. Dated samples are mainly of millimeter- to centimeter-scale botryoidal Fe-oxides, with a few samples of Fe-oxide cement (Figs. 2G and 2H).

## SAMPLES AND METHODS

### Sample Selection

Our sample preparation methods were designed to minimize the fraction of material other than Fe-oxide and Mn-oxide in our analyzed aliquots. Fe-oxide aliquots consisted of mostly micro- to millimeter-scale botryoidal material found in cements and as fracture-fill material. Fe-oxide cement comprises three different textures: mostly microscale botryoids, plate-shaped Fe-oxides that appear to be radiating from botryoids, and rectangular (resembling the shape of French fries) crystals seen in two samples. It is likely that analyzed aliquots from cement samples contained varying proportions of all these textures and compositions. Mn-oxide aliquots also comprise three main textures: dense near-end-member Mn-oxide material consisting of many plate-like aggregates (observed in both cement and fracture-fill material), needle-like crystals of Ba-rich Mn-oxide, and fibrous Ba-rich Mn-oxide. The latter two textures are only observed in cement material. Oxide textures are further described in the section on "Petrographic and SEM Observations." Cement samples that were collected and picked for (U-Th)/He dating were rich in either Fe or Mn and, in a few cases, contained similar amounts of each element. Fracture-fill samples that were collected and picked for (U-Th)/He dating were either Fe- or Mn-oxide near end members, but not both.

Fe- and Mn-oxide cements were purified by crushing using a mortar and pestle to separate the cement matrix from quartz and feldspar grains. After crushing, the material was cleaned with ethanol to remove any clay material

on grain surfaces. After drying, samples were passed through a Frantz isodynamic magnetic separator to further remove unwanted detrital or nonoxide cement material. We used a high-power optical Leica MZ16 microscope to identify relatively pure cement aliquots for analysis and to take photomicrographs to measure dimensions of selected material. Selected materials were then placed in ethanol and packed into 1 mm Nb tubes. Most aliquots consisted of 1 to 5 mm fragments of oxides (consisting of many microscale crystals), in an effort to provide an adequate amount of material for analysis, though this also increased the likelihood of including phases other than Fe- and Mn-oxide.

Analyzed fracture-fill material consisted of dense, botryoidal Fe-oxides and both dense Ba-rich Mn-oxide and near-end-member Mn-oxide phases. SEM observations helped to distinguish the two Mn-oxide phases. Once they were recognized, we were able to tell them apart by color; black for Ba-rich Mn-oxide phase and silver/metallic for near-end-member Mn-oxide phase, although most aliquots consisted of both phases due to the difficulty in separating fine-grained materials. Fe- and Mn-oxides were removed from their respective veins using rotary tools and were then crushed to get smaller samples into Nb tubes. Fracture-fill material was also cleaned using ethanol and allowed to dry but did not require magnetic separation. Selected aliquots of fracture-fill material were then packed into Nb tubes using the same method as for cement aliquots.

Parent nuclide and minor- and trace-element concentrations in undegassed aliquots of Fe- and Mn-oxide samples were also analyzed to understand effects of laser heating on compositions of aliquots during exposure to high-temperature He extraction. Undegassed aliquots were selected from the same pool of aliquot material as dated aliquots. These aliquots were packed into Nb tubes the same way as dated material, but they were not subjected to He extraction (described below) prior to dissolution.

### Petrographic and SEM Observations

We examined polished thick sections of samples using a high-power (160 $\times$ ) optical Leica MZ16 stereozoom microscope and a Hitachi 3400N SEM equipped with an Oxford EDS/electron backscatter diffraction (EBSD) system. We acquired backscattered electron (BSE) and secondary electron (SE) images of thick sections and sample fragments, along with energy-dispersive (EDS) maps, to aid in our aliquot selections. We used a Thermo Nicolet Almega micro-Raman spectrometer to identify Fe- and Mn-oxides from veins in the north fault.

Raman spectrometry identified botryoidal Fe-oxides as goethite. Identification of Mn-oxide minerals was difficult due to their fine grain size, but we did identify needle-like material as hollandite. The more metallic and relatively pure Mn-oxide in the veins is pyrolusite.

Samples 13PRCP8 and 14VGCPI0 from the north fault consist of an ~5-mm-thick subvertical vein with botryoidal Fe-oxide at the rims, a transitional Ba-rich Mn-oxide, and a central portion of relatively pure Mn-oxide. A similar sequence of adjacent phases is observed in cement as well. Ba-rich Mn-oxide emanates from the surface and fractures in larger botryoids toward the center and is also observed in smaller botryoids near the top of the vein (Fig. 3A). Upon examination, Fe-oxide fracture-fill material showed little or no mineralogic heterogeneity, whereas Ba-rich Mn-oxides showed a slight K enrichment (likely cryptomelane) compared to other Fe- and Mn-oxides. This was observed in all Ba-rich Mn-oxide samples collected in this study, including cement samples.

Fe-oxide cement (dark red) dominates and transitions into Mn-oxide cement (black/silver mixture) with distance from fracture-fill material. Detrital grains in cement samples are mainly quartz, with lesser amounts of feldspar and other minerals. Oxide cement shows a pattern of Fe-oxide rimming sand grains, which is overlain by Ba-rich Mn-oxide, which is in turn overlain by relatively pure Mn-oxide cement farthest from grains. Textures of north fault cement samples consist of micrometer- and millimeter-scale botryoidal Fe-oxides as cement and fracture-fill material, Ba-rich Mn-oxide in microscale needles/fibers, which in some areas are so dense the needles are no longer visible, and very dense relatively pure Mn-oxides containing microscale sheets/blades (Fig. 3E).

All samples from the south fault are Fe- and Mn-oxide cement. Samples collected farthest away from the fault consist of Fe-oxide cement, whereas samples closest to the fault consist of Ba-rich Mn-oxide and relatively pure Mn-oxide. Textures are similar to those observed in the north fault but are much finer grained (Fig. 3). Very smooth, relatively pure Mn-oxide is found throughout many of the samples and is typically adjacent to Ba-rich Mn-oxides, which also show needle-like/fibrous textures similar to those in the north fault. Individual needles/fibers of these Mn-oxide crystals are no more than 1  $\mu$ m thick. Fe-oxides from the south fault are mostly microscale botryoids; French fry textures are observed in some samples, and very fine blade-shaped aggregate crystals radiate from some botryoids (Fig. 3). Fe-oxide samples picked for (U-Th)/He dating from the south fault are mostly botryoidal cement, but due to

the fine-grained nature of the different textures, various textures and compositions may be present in individual aliquots. The same is true for Mn-oxides, in which both Ba-rich Mn-oxide and relatively pure Mn-oxide are likely present in aliquots.

Samples from the east fault are primarily Fe-oxide cement and botryoids, though some rare Mn-oxide cement is also present (Fig. 3). SEM imaging shows no difference in chemical signature between the orange-to-red color variations. These color differences appear to be due to the quantity of Fe-oxide in a given location (e.g., dark-red Fe-oxide cement is due to large dense concentrations of Fe, whereas orange cement has less Fe-oxide in it; Fig. 3). The Mn-oxide in east fault samples is Ba-rich Mn-oxide and has the same needle-like/fibrous textures observed in samples from other faults in the study.

### (U-Th)/He Analyses

The  $^4\text{He}$  measurement process used here is the same as Fe- and Mn-oxides dated by Evenson et al. (2014) and Reiners et al. (2014). Aliquots of samples were loaded into Nb tubes, loaded in an ~42 well Cu planchet, and then loaded into a UHV (ultra high vacuum) gas extraction line and heated to temperatures of ~850–1000 °C (low to medium glow in visible range) for 15 min for both Fe- and Mn-oxides using a Nd-YAG or diode laser. Low temperatures were necessary to prevent the loss of samples at higher temperatures and to avoid volatilization of elements later quantified by inductively coupled plasma–mass spectrometry (ICP-MS). Experiments at varying lasing intensity, as well as on undegassed aliquots, were also performed to account for possible volatilization of elements. Each aliquot was then reheated a second time for a period and lasing intensity slightly higher in duration and in temperature than the first to confirm  $^4\text{He}$  had been quantitatively extracted. The majority of Fe-oxides and Mn-oxides required just one reheating period to extract all  $^4\text{He}$ , but a few required multiple degassing extractions. One sample requiring multiple extractions yielded a much older age, likely due to the presence of a detrital phase (such as apatite) with high U, Th, and He. Some aliquots did not receive a second heating as part of an experiment to (1) see whether ages would be affected by the amount of extracts performed and (2) test for volatilization of elements at higher temperatures and durations during multiple extractions.

Following He measurement, aliquots were transferred to polytetrafluoroethylene (PTFE) vials for Parr-bomb dissolution and U-Th measurements by isotope dilution using an Element2 high-resolution ICP-MS, as described by

Reiners (2005). The same process was used for undegassed samples, but with a Nb tube added prior to dissolution. Following the approach of Reiners et al. (2014), we did not make corrections for alpha ejection on Fe- and Mn-oxide fracture-fill samples because the samples have dimensions that far exceed the length scale of alpha stopping distances. In the case of cement-dominated samples, an alpha ejection correction was not made due to variations in cement length scales and the relatively small corrections that would be required.

The same solutions used for U-Th isotope-dilution measurements were also used to measure bulk element compositions in samples by ICP-MS. Solutions contained dissolved sample aliquots of Fe- or Mn-oxide, along with their Nb tubes, as well as the  $^{233}\text{U}$ - $^{229}\text{Th}$  spike used to measure U and Th isotopes, plus any other phases present as inclusions or interstitial material.

Analyses are reported in Tables 1, 2, and 3 as total masses or moles rather than concentrations because aliquots were not weighed before analysis. However, to estimate concentrations of elements, as in previous studies, we assumed that the majority of the matrix was either Fe- and/or Mn-oxide, so the approximate molar concentrations of an element could be estimated from its ratio to the normalized sum of Fe and Mn (Evenson et al., 2014; Reiners et al., 2014). To avoid referring an Fe- or Mn-oxide to a particular mineral formula, we used these “molar ratios, mole percent (mol%), or micromole fractions (ppm).” Our molar ratios of each element are only representative of the actual specimen if elements, including Fe and/or Mn, were not lost by volatilization or other processes during  $^4\text{He}$  extraction. Previous studies have observed volatilization of U during  $^4\text{He}$  extraction, which results in increased Th/U ratios and older He ages in goethite

when samples are heated to temperatures above 1000 °C (Vasconcelos et al., 2013; Danišik et al., 2013; Evenson et al., 2014; Reiners et al., 2014). We used the concentrations of relatively volatile elements in undegassed aliquots as one way to assess the possible effects of open-system behavior during laser heating and analysis. Aliquots used for heating-intensity experiments were heated for 8 min at varying glows and were not subjected to a second extraction. Experiments performed in this study suggest that at certain temperatures, Fe, Mn, and U were volatilized in some cases. Results presented here from experiments other than those just described all used lower extraction temperatures (~850 °C) to avoid sample decomposition/melting and loss.

### (U-Th)/He Step-Heating Experiments

To interpret our (U-Th)/He ages and to quantify the kinetics of He diffusion in representative, polycrystalline samples, we performed step-heating He release experiments on one Fe-oxide and one Mn-oxide aliquot from sample 13PRCP8, the ~1-cm-thick vein from the north fault. This followed procedures described in Shuster and Farley (2004), Shuster et al. (2005), and Evenson et al. (2014). To ensure a spatially uniform distribution of the diffusant ( $^3\text{He}$ ) throughout the samples, they were irradiated with a beam of ~220 MeV protons for 5 h and a total fluence of  $\sim 1 \times 10^{16}/\text{cm}^2$  at the Francis H. Burr Proton Therapy Center at Massachusetts General Hospital, Boston, Massachusetts. After irradiation, ~0.15 mg polycrystalline aliquots of each sample were placed in direct contact with a type K thermocouple under ultrahigh vacuum and degassed under controlled thermal conditions using a feedback-controlled laser diode; the  $^4\text{He}/^3\text{He}$  ratio and molar abundance of  $^3\text{He}$

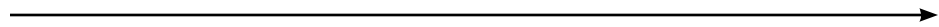


**Figure 3 (on following page).** Petrographic and scanning electron microscope (SEM) images of representative samples from all faults in this study. (A) Petrographic image of 14VGC10 thick section showing a 0.5-cm-thick vein containing Fe- and Mn-oxides. Botryoidal black masses at top (thin) and bottom (thick) of vein are Fe-oxides; black dendritic material that appears to be emanating from the bottom botryoidal layer is Ba-rich Mn-oxide transitioning into a thin layer of Mn-oxide with less Ba; gray prismatic material in center of vein is near-end-member Mn-oxide. (B) SEM image of thick section shown in A. (C) SEM image of section in B with grayscale colors corresponding to oxide type: black—Fe-oxide, white—Ba-rich Mn-oxide, gray—near-end-member Mn-oxide. (D) Botryoidal Fe-oxide cement surrounding quartz grains. (E) Needle-like Ba-rich Mn-oxide and dense near-end-member Mn-oxide in fracture-fill material. (F) Needle-like Ba-rich Mn-oxide and dense near-end-member Mn-oxide in cement material. (G) Fibrous Ba-rich Mn-oxide made up of many finer-grained needles. (H) Microscale botryoidal Fe-oxide. (I) French fry Fe-oxide texture present as cement between quartz grains. (J) Thin blades of Fe-oxide emanating from larger botryoidal Fe-oxide cement. (K) Thick section of Fe-oxide (left to right) and Mn-oxide (right) cement; 500 μm scale. (L) SEM image of section in K showing higher concentration of Fe-oxide from right to left. Needle-like material to the right is Ba-rich Mn-oxide.

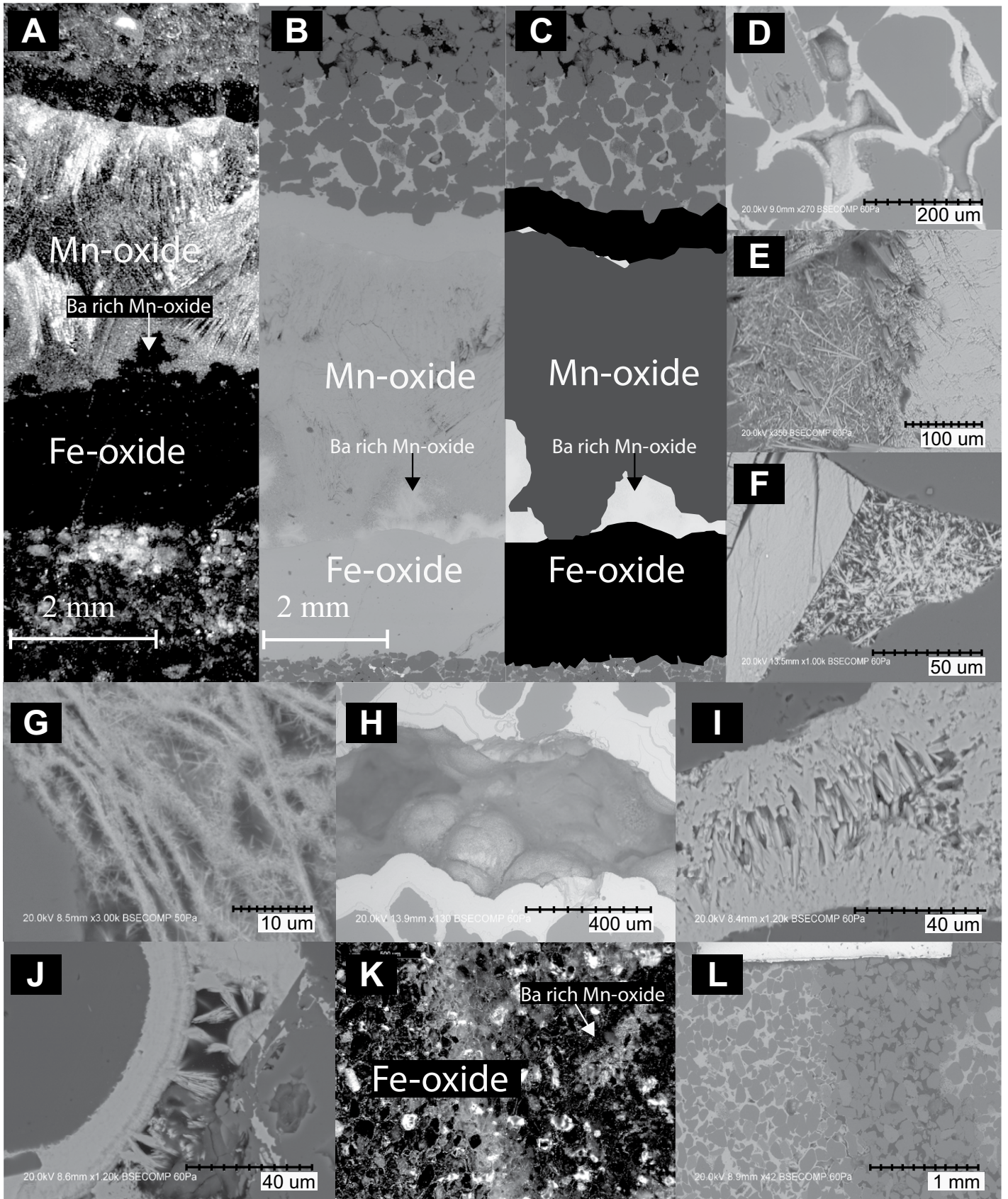


Figure 3.







TABLE 3. EAST FAULT (U-Th)/He AND COMPOSITIONAL DATA

Sample name	He (fmol)	±1σ (fmol)	U (ng)	±1σ (ng)	Th (ng)	±1σ (ng)	Th/U	Raw date (Ma)	±1σ date (Ma)	%	Fe (μmol)	Mn (μmol)	Fe+Mn (μmol)	Mn/(Fe+Mn) (molar ratio)	U (μmol)	Th (μmol)	U/(Fe+Mn) (molar ratio)	Th/(Fe+Mn) (molar ratio)	eU/(Fe+Mn) (μmol/mole)	
14VGGP11																				
15C051_VG_14VGGP11_bot1	8.38	0.116	0.282	0.0041	0.0031	0.0010	0.0115	5.50	0.11	2.0	0.67170	0.00322	0.675	0.9952	1.185E-06	1.358E-08	1.755E-06	2.011E-08	1.760E-06	1.760
15C052_VG_14VGGP11_bot2	2.70	0.068	0.069	0.0010	0.00249	0.00038	0.3672	6.65	0.19	2.8	0.24979	0.00309	0.253	0.9878	2.920E-07	1.072E-07	1.155E-06	4.240E-07	1.254E-06	1.254
15C053_VG_14VGGP11_bot3	2.00	0.066	0.086	0.0013	0.0024	0.00006	0.0291	4.31	0.15	3.6	0.17518	0.00089	0.176	0.9950	3.600E-07	1.046E-08	2.044E-06	5.942E-08	2.058E-06	2.058
14VGGP12A																				
15B295_VG_14VGGP12A_cm1	0.10	0.048	0.016	0.0003	0.0024	0.00010	0.1539	1.07	0.54	50.2	0.00053	0.01418	0.015	0.0359	6.800E-08	1.047E-08	4.623E-06	7.115E-07	4.791E-06	4.791
15B296_VG_14VGGP12A_cm2	0.13	0.048	0.014	0.0003	0.0030	0.00010	0.2255	1.66	0.63	37.9	0.00488	0.01829	0.023	0.2105	5.736E-08	1.293E-08	2.476E-06	5.583E-07	2.607E-06	2.607
15B296a_VG_14VGGP12A_cm3	0.05	0.046	0.011	0.0003	0.0043	0.00008	0.4127	0.84	0.72	85.7	0.00184	0.00682	0.009	0.2120	4.527E-08	1.869E-08	5.229E-06	2.158E-06	5.736E-06	5.736
15B297_VG_14VGGP12A_cm4	0.46	0.058	0.024	0.0004	0.0127	0.00029	0.5414	3.14	0.40	12.8	0.00279	0.02468	0.027	0.1014	1.009E-07	5.463E-08	3.674E-06	1.989E-06	4.141E-06	4.141
15B312_VG_14VGGP12A_cm5	0.24	0.042	0.023	0.0004	0.0035	0.00007	0.1551	1.85	0.33	17.8	0.00076	0.02465	0.025	0.0297	9.690E-08	1.502E-08	3.814E-06	5.913E-07	3.952E-06	3.952
14VGGP12B																				
15B298_VG_14VGGP12B_fx1	1.72	0.060	0.214	0.0031	0.0031	0.00007	0.0149	1.49	0.06	3.8	0.28206	0.00060	0.283	0.9979	8.992E-07	1.339E-08	3.181E-06	4.737E-08	3.192E-06	3.192
15B299_VG_14VGGP12B_fx2	4.05	0.091	0.521	0.0077	0.0019	0.00006	0.0038	1.44	0.04	2.7	0.54663	0.00118	0.548	0.9978	2.187E-06	8.362E-09	3.992E-06	1.526E-08	3.996E-06	3.996
15B300_VG_14VGGP12B_fx3	4.26	0.075	0.523	0.0076	0.0054	0.00015	0.0105	1.51	0.03	2.3	0.64072	0.00143	0.642	0.9978	2.198E-06	2.312E-08	3.419E-06	3.601E-08	3.428E-06	3.428
15B301_VG_14VGGP12B_fx1	3.22	0.069	0.603	0.0089	0.0046	0.00010	0.0078	0.99	0.03	2.6	0.34007	0.00445	0.345	0.9971	2.534E-06	1.987E-08	7.356E-06	5.769E-08	7.370E-06	7.370
15B302_VG_14VGGP12B_fx2	1.17	0.056	0.123	0.0018	0.0076	0.00015	0.0631	1.74	0.09	4.9	0.07316	0.01270	0.086	0.8521	5.171E-07	3.261E-08	6.023E-06	3.799E-07	6.112E-06	6.112
15B304_VG_14VGGP12B_fx3	4.02	0.075	0.108	0.0018	0.0265	0.00045	0.2511	6.52	0.16	2.4	0.01105	0.25584	0.267	0.0414	4.544E-07	1.141E-07	1.702E-06	4.274E-07	1.803E-06	1.803
15B305_VG_14VGGP12B_cm1	0.09	0.040	0.004	0.0003	0.0026	0.00009	0.5944	3.30	1.49	45.0	0.00220	0.00007	0.002	0.9678	1.850E-08	1.099E-08	8.144E-06	4.841E-06	9.282E-06	9.282
15B306_VG_14VGGP12B_cm2	0.27	0.046	0.027	0.0005	0.0078	0.00018	0.3009	1.76	0.30	17.0	0.00117	0.04334	0.045	0.0264	1.123E-07	3.380E-08	2.524E-06	7.594E-07	2.702E-06	2.702
15B307_VG_14VGGP12B_cm3	0.46	0.045	0.020	0.0004	0.0078	0.00014	0.4024	3.91	0.39	10.1	0.00463	0.05849	0.063	0.0734	8.330E-08	3.352E-08	1.320E-06	5.310E-07	1.444E-06	1.444
14VGGP12C																				
15B308_VG_14VGGP12C_fx1	0.59	0.044	0.043	0.0007	0.0115	0.00019	0.2727	2.38	0.18	7.6	0.00537	0.01929	0.025	0.2176	1.822E-07	4.968E-08	7.390E-06	2.015E-06	7.863E-06	7.863
15B309_VG_14VGGP12C_fx2	2.32	0.073	0.174	0.0026	0.0030	0.00013	0.0175	2.47	0.09	3.5	0.27015	0.00167	0.272	0.9939	7.314E-07	1.277E-08	2.691E-06	4.700E-08	2.702E-06	2.702
15B310_VG_14VGGP12C_fx3	5.27	0.103	0.411	0.0061	0.0076	0.00016	0.0189	2.37	0.06	2.4	0.58380	0.00348	0.587	0.9941	1.726E-06	3.261E-08	2.938E-06	5.553E-08	2.951E-06	2.951
Cynthia																				
15A458_PR_Cynthia_A_nod_1	1.16	0.067	0.379	0.0054	0.0077	0.00017	0.0207	0.56	0.03	6.0	2.41972	0.00666	2.427	0.9972	1.593E-06	3.305E-08	6.567E-07	1.362E-08	6.599E-07	0.660
15A459_PR_Cynthia_A_nod_2	1.89	0.077	0.632	0.0090	0.0089	0.00029	0.0144	0.55	0.02	4.3	3.84124	0.01304	3.854	0.9966	2.654E-06	3.815E-08	8.866E-07	9.898E-09	6.909E-07	0.691
15A460_PR_Cynthia_A_nod_3	2.49	0.083	0.766	0.0110	0.0114	0.00019	0.0152	0.60	0.02	3.6	0.79591	0.00240	0.798	0.0030	3.218E-06	4.898E-08	4.031E-06	6.135E-08	4.045E-06	4.045

Note: Sample data in bold were included in the age plots due to low % error <-5% and/or Th/U <-0.01 for fracture-fill material; Th/U <-0.10 for cement samples.

in the evolved gas at each step were measured using sector field mass spectrometry. Full analytical procedures for gas processing and mass spectrometry can be found in Tremblay et al. (2014a,b).

### Ar Analyses

We performed a step-heating <sup>40</sup>Ar/<sup>39</sup>Ar experiment on Mn-oxide from sample 13PRCP8, the central Mn-oxide from the north fault. Using rotary tools, Mn-oxide was removed from a vein that contained Fe-oxide as well. Handpicking, using a microscope, ensured all unwanted material was removed from the sample. The remaining mineral separate was a mixture of pure-phase Mn-oxide end member (pyrolusite) and a Ba-rich Mn-oxide (hollandite), which contained microscale crystals of cryptomelane.

The separate was packaged in Cu foil, sealed into an evacuated quartz tube, and irradiated in the central thimble of the U.S. Geological Survey TRIGA reactor in Denver, Colorado, for 3 h. Cadmium shielding was employed to reduce nuclear interferences on <sup>40</sup>Ar from <sup>40</sup>K. Packets of GA1550 biotite (98.79 ± 0.54 Ma; Renne et al., 1998) were interspersed between samples in the quartz tube to monitor the neutron flux during irradiation.

During a previous attempt to analyze a larger aliquot of 13PRCP8, we discovered that this sample contained large quantities of active gases that evolved during the early heating steps, overloading the gas purification systems and producing significant pressure scattering in the mass spectrometer. For the second attempt, we preheated the sample packet under vacuum at 200 °C for 48 h to help remove the loosely bound gas fraction, and then we degassed it in 12 steps using a double-vacuum resistance furnace connected to a fully automated extraction line. The gas evolved from each step was purified using SAES getters operated at 450 °C and 20 °C, and a liquid-nitrogen-cooled cold finger. The purified argon was analyzed in a Thermo Scientific ARGUS VI multicollector mass spectrometer. The five argon isotopes were measured simultaneously using Faraday detectors equipped with a 10<sup>13</sup> Ω feedback resistor for <sup>39</sup>Ar and 10<sup>12</sup> Ω resistors for <sup>40</sup>Ar, <sup>38</sup>Ar, <sup>37</sup>Ar, and <sup>36</sup>Ar. The isotope abundance measurements were corrected for extraction line blank, mass discrimination, and nuclear interferences on Ar isotopes from Ca and K. Mass spectrometer discrimination was monitored by repeat analyses of atmospheric argon, which yielded an average <sup>40</sup>Ar/<sup>36</sup>Ar value of 297.75 ± 0.28 during the period of the step-heating experiment. Ages and other analytical results were generated using ArArCalc version 2.52 (Koppers, 2002).

## RESULTS

### Trace-Element Chemistry

U and Th (molar) concentrations for most fracture-fill material, for both Fe- and Mn-oxide samples, had ranges of ~1–20 ppm and ~0.01–0.50 ppm, respectively. One dated sample in particular, 14VGCP10U\_MnC, had high Th concentrations of ~10–170 ppm, whereas its U concentration ranged ~7–13 ppm. U and Th concentrations for most cement material had ranges of ~1–5 ppm and ~0.2–1 ppm, respectively.

All dated and undegassed fracture-fill aliquots were near end-member Fe- or Mn-oxide (>90–99 mol%), with the exception of four aliquots (13PRCP8U\_13, 13PRCP8U\_14, 14VGCP10L\_4, and 14VGCP12C\_fx11; <80 mol%), which were a mixture of both Fe- and Mn-oxides. Nearly all dated and undegassed cement aliquots were near-end-member Fe- or Mn-oxide, with the exception of two aliquots (14VGCP12A\_cm2 and 14VGCP12A\_cm3; <80 mol%).

Ni concentrations were higher in cement material, 0.003–0.05 mol%, than most fracture-fill material,  $10^{-4}$  to 0.002 mol%. The highest Ni concentrations were observed in Fe-oxide frac-

ture-fill material from the east fault (0.004–0.15 mol%). Cement material had higher Al concentrations, from 0.1 to 10 mol%. Higher Al concentrations in cement material might reflect either higher concentrations in this type of material or Al contributed by detrital phases.

Fracture-fill aliquots were used to control for volatilization of relatively volatile elements in dated and undegassed aliquots as one way to assess the possible loss of material during laser heating and analysis (Fig. 4). Figure 4A demonstrates how heating intensity affected Fe- and Mn-oxide aliquots during He extraction. Most aliquots did not experience Fe- or Mn- volatilization, but in most cases in which He was extracted at high lasing intensities (>1100 °C; red symbols), both Fe and Mn were volatilized and lost from the aliquots. If Fe and Mn are lost during He extraction to some degree, this will affect how individual aliquots plot when element concentrations are normalized to relative Fe + Mn, as used in Reiners et al. (2014) and Evenson et al. (2014). Low lasing intensity (~850 °C) extractions appear to remove all He from samples without the sample loss that occurs at higher temperatures.

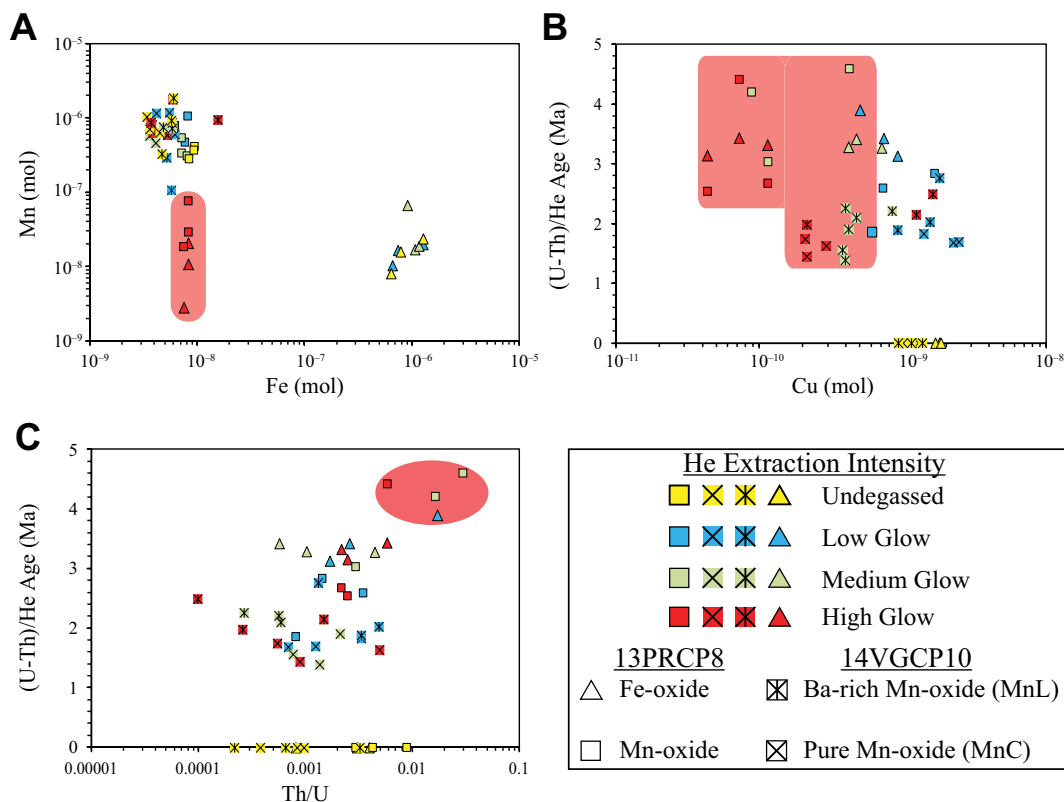
Cu is a much more volatile element than Fe and Mn, and it allows us to observe volatilization at different heating intensities. Figure 4B shows

(U-Th)/He ages plotted against Cu content. Undegassed Cu aliquots had Cu content of  $\sim 10^{-9}$  mol, as did most aliquots subjected to low-intensity extractions (blue symbols). Aliquots exposed to higher-intensity extractions appeared to have about ten times less Cu. The Cu content of each aliquot does not appear to be related to (U-Th)/He age. Other volatile elements, including Pb and Zn, also appear to have been strongly volatilized during high-intensity (>1100 °C) extractions. In particular, we used Cu, which is volatilized at temperatures >>1000 °C, to control for possible volatilization of other elements of interest such as U and Th. Using this information, we determined that there is evidence for volatilization of U in four dated aliquots (all older than 3.6 Ma; Fig. 4C), resulting in increased Th/U, which is correlated with older (U-Th)/He ages observed in other studies in which He was extracted at high temperatures (Danišik et al., 2013; Vasconcelos et al., 2013; Reiners et al., 2014).

### (U-Th)/He Analyses

Figure 5A shows (U-Th)/He ages for all dated aliquots, from all locations, along with their  $1\sigma$  analytical uncertainty, as a function of eU (U + 0.235Th), represented in pmol. Cement samples

**Figure 4. Elemental compositions of dated and undegassed Fe- and Mn-oxide aliquots used to understand volatilization during laser heating. Molar concentrations are reported in these plots. (A) Molar Mn and Fe contents. Most fracture-fill aliquots from the north fault lost Fe or Mn when He was extracted at low (blue) to medium (green) intensities, as evident in undegassed samples (yellow). Samples heated to higher extraction temperatures (>1100 °C) have much lower Fe and Mn content. Concentrations of other elements reported relative to Fe + Mn are compromised in such cases. (B) (U-Th)/He age vs. Cu. Cu is a relatively volatile element and was used to check for volatilization of other elements. Aliquots from which He was extracted at medium to high temperatures have significantly lower Cu contents. (C) (U-Th)/He age vs. Th/U. Most dated and undegassed aliquots have Th/U values of 0.0002–0.01, regardless of heating temperature during extraction. Four aliquots with varying heating intensity extractions appear to have lost more U relative to Th and have older ages.**



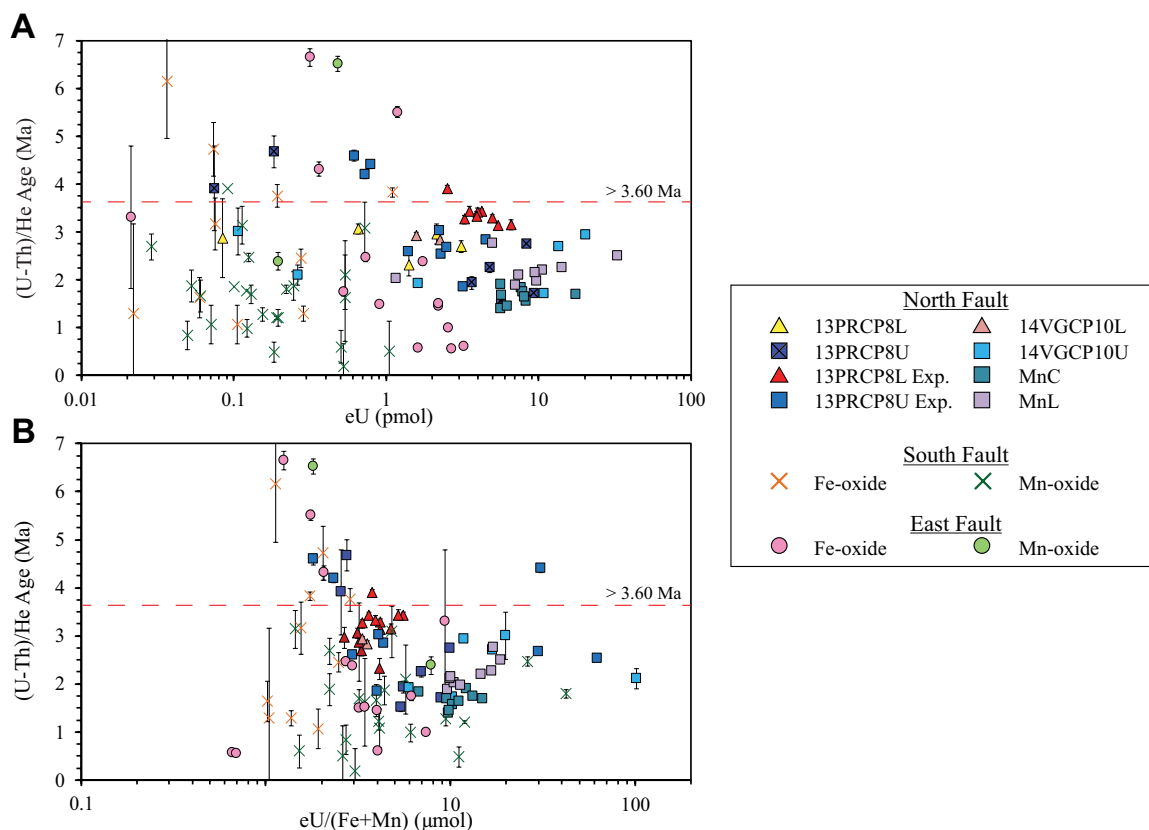


**Figure 5.** (U-Th)/He ages as a function of eU ( $U + 0.235Th$ ) contents (pmol) and concentration (micromole with respect to Fe + Mn). All dated aliquots from all three faults are shown, including those with high Th/U and high uncertainties ( $1\sigma$ ). (A) (U-Th)/He ages plotted against eU (pmol). Majority of dated aliquots are younger than 3.6 Ma. Cement aliquots (south fault) have the highest uncertainties ( $\sim 10\%$ – $40\%$ ); in contrast, fracture-fill material aliquots have very low uncertainties ( $< 5\%$ ). Cement aliquots (“X” symbol) have the lowest eU content, ranging from 0.02 to 1 pmol. Fracture-fill material aliquots from the north fault have high eU values, specifically Mn-oxide aliquots, which have eU values of 5–20 pmol. Fracture-fill material aliquots from the east fault have eU values of 0.2–4 pmol. (B) (U-Th)/He ages plotted against eU/(Fe + Mn) ( $\mu\text{mol}$ ; ppm). Cement aliquots have the lowest eU content, ranging from 1 to 7 ppm. Fracture-fill material aliquots from the north fault have high eU values, specifically Mn-oxide aliquots, which have eU values of 5–20 ppm. Fracture-fill material aliquots from the east fault have eU values of 0.7–6 ppm.

had higher uncertainties, due to low parent and daughter contents, than fracture-fill material. There is no clear correlation between (U-Th)/He age and eU other than a wide range of ages at lower eU; cement eU values ranged from 0.02 to 1 pmol, and most fracture-fill material eU values ranged from 1 to 20 pmol. When eU values were normalized to Fe + Mn, eU values in most dated aliquots increased due to the possible volatilization of Fe and/or Mn (Fig. 5B).

Relatively pure vein material from the north fault had ages with the lowest uncertainties, lowest Th/U, and typically the highest eU content. In contrast, most cement samples had higher Th/U, and within this group, samples with the highest Th/U had the oldest ages, including some greater than 3.6 Ma. This, combined with the relatively low Th/U of the pure fracture-fill material, sug-

gests that high Th/U is likely due to the presence of detrital components in the aliquot. In general, samples with high Th/U also had higher uncertainties (i.e.,  $> 5\%$  to  $20\%$ ). Based on these observations, we omitted samples from the north and east fault from further consideration if they had greater than  $5\%$  uncertainty ( $1\sigma$ ) and Th/U  $> 0.01$ . The higher average uncertainties and Th/U of cement material required a different screening process. On average, cement samples associated with high Th/U ( $> 0.20$ ) had much older ages and high uncertainties ( $\sim 20\%$ ). (U-Th)/He ages of remaining samples were plotted in probability versus He ages (Fig. 6), used for bulk age calculations, and ranged from 0.50 to 3.43 Ma (Tables 1, 2, and 3).

Samples from the relatively pure vein in the north fault region provided the most reproduc-

ible He ages (Table 1). Dated Mn-oxide aliquots from the north fault ranged from 2.93 to 1.39 Ma, with one outlier with an age of 4.41 Ma, whereas botryoidal Fe-oxide aliquots ranged from 3.43 to 2.84 Ma. These oxides had eU concentrations of  $\sim 1$ – $4$  pmol for Mn-oxides and  $3$ – $8$  pmol for Fe-oxides. The Ba-rich Mn-oxide phase (14VGCP10U\_MnL) had ages of 2.76–1.88 Ma, whereas the relatively pure phase Mn-oxide (14VGCP10U\_MnC) had younger ages of 1.90–1.39 Ma (Fig. 4). Dated aliquots from sample 14VGCP10 had the highest eU content out of all the dated oxides across all faults, with concentrations that ranged from 6 to 20 pmol.

South fault sample data (Table 2) ranged from 3.16 to 0.50 Ma, with two outliers with ages of 3.82 and 4.72 Ma. The majority of the aliquots in this age range were Mn-oxide aliquots, with

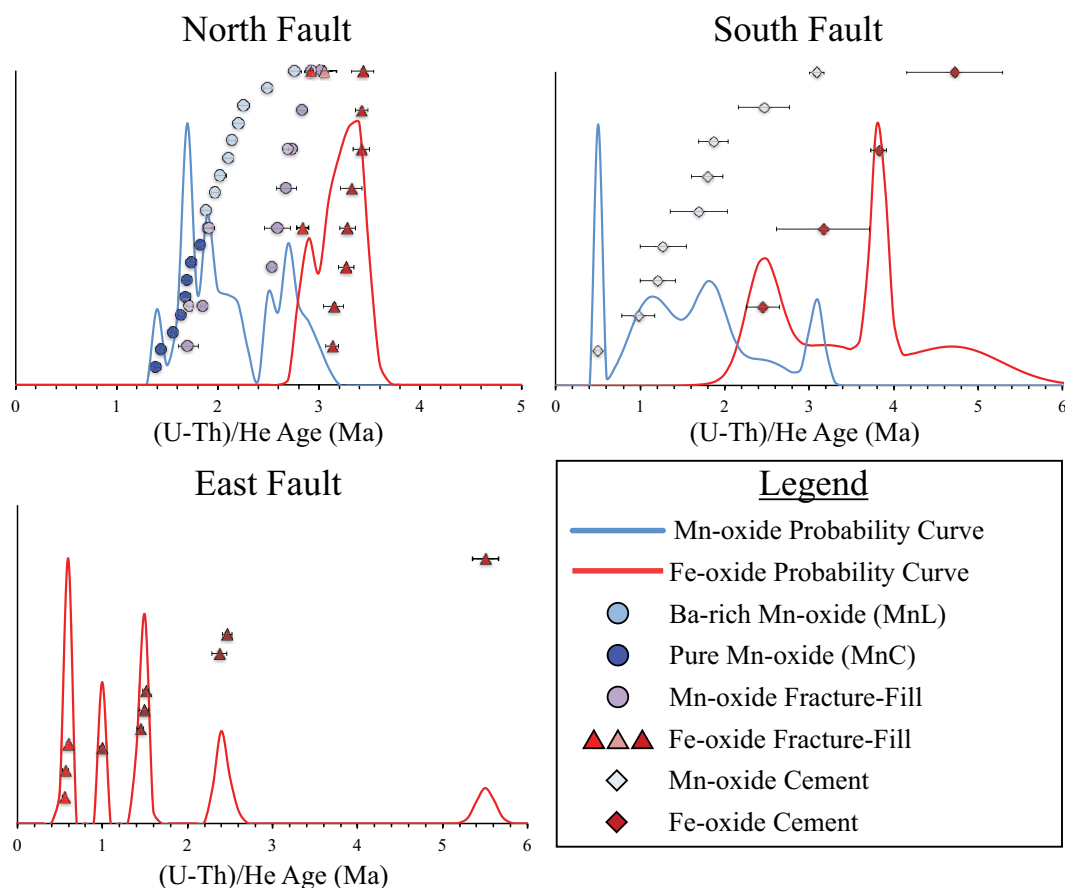


**Figure 6.** Relative probability plots of Fe- and Mn-oxide (U-Th)/He dates. Solid blue lines are probability curves for Mn-oxides; red blue lines are probability curves for Fe-oxides. Samples in varying blue colors represent Mn-oxides; samples in varying red colors represent Fe-oxides. Error bars on data points represent  $1\sigma$  uncertainty.

the exception of the two outliers and one aliquot, with an age of 3.16 Ma, which were Fe-oxides. Fe- and Mn-oxide eU content were the lowest observed values and ranged from 0.02 to 1 pmol, with the highest content seen in Mn-oxides. He ages for botryoidal Fe-oxides from the east fault ranged from 2.47 to 0.55 Ma, with one outlier with an age of 5.50 Ma (Table 3). Fe- and Mn-oxide eU contents ranged from 0.2 to 4 pmol.

### He Diffusion Experiments

Results of  $^4\text{He}/^3\text{He}$  step-heating diffusion experiments on proton-irradiated polycrystalline aliquots are shown in Table 4, Figure 7 (Arrhenius plots), and Figure 8 (age spectra figures). Neither sample showed a simple Arrhenius relationship when values of  $D/a^2$  were calculated from the release fractions of  $^3\text{He}$  (Fig. 7; Fechtig and Kalbitzer, 1966). Instead, each can be explained by simultaneous outward diffusion of  $^3\text{He}$  from a large number of crystallites spanning a range in sizes. To interpret the diffusion results, we optimized multiple diffusion domain models to predict the observed  $^3\text{He}$  release data. We prescribed either three (for Mn-oxide) or four (for Fe-ox-

ide) spherical model domains, and we allowed  $E_a$  of all domains,  $D_0/a^2$ , and the relative gas fractions within each domain to be free variables. Using a Monte Carlo search algorithm (Tremblay et al., 2014a,b), we identified the set of parameters that minimized the misfit between predicted and calculated values of  $D/a^2$  and the gas proportions of each analysis. The sets of best-fit parameters are described next, are given in Table 5, and are shown in Figure 7.

The Mn-oxide aliquots showed an Arrhenius trend consistent with multidomain behavior similar to the results for other Mn-oxides (Lippolt and Hautmann, 1995; Reiners et al., 2014). A diffusion model with three domains with identical apparent  $E_a$  of 130 kJ/mol (similar to  $E_a$  of 134 kJ/mol from Lippolt and Hautmann, 1995) and  $\ln(D_0/a^2)$  of 20, 30, and 10  $\ln(\text{s}^{-1})$ , in proportions of 86%, 7%, and 7%, respectively, predicted the observed Arrhenius relationship of the sample (Fig. 7). Although we recognize that  $T_c$  does not carry its usual meaning in this case, because of the likelihood of formation of some domains at low temperatures, it still provides a convenient index of bulk retentivity to compare with other minerals. The apparent closure

temperatures of these domains (assuming a cooling rate of 10  $^{\circ}\text{C}/\text{m.y.}$ ) ranged from 14  $^{\circ}\text{C}$  for  $\ln(D_0/a^2)$  of 20  $\ln(\text{s}^{-1})$ , to  $-22$   $^{\circ}\text{C}$  for  $\ln(D_0/a^2)$  of 30  $\ln(\text{s}^{-1})$ , to 86  $^{\circ}\text{C}$  for  $\ln(D_0/a^2)$  of 10  $\ln(\text{s}^{-1})$ . The combined weighted average  $T_c$  for all domains would be  $\sim 17$   $^{\circ}\text{C}$ .

The Fe-oxide aliquots also showed multidomain behavior consistent with previous results on diagenetic goethite and hematite (Shuster et al., 2005; Heim et al., 2006; Reiners et al., 2014). Best-fit modeling using a simple model with four domains with identical  $E_a$  of 159 kJ/mol required domains with  $\ln(D_0/a^2)$  of 15  $\ln(\text{s}^{-1})$ , 27.5  $\ln(\text{s}^{-1})$ , 19  $\ln(\text{s}^{-1})$ , and 39  $\ln(\text{s}^{-1})$ , in proportions of 75%, 9%, 9%, and 7%, respectively. These domains corresponded to apparent closure temperatures of 51  $^{\circ}\text{C}$  for  $\ln(D_0/a^2)$  of 15  $\ln(\text{s}^{-1})$ ,  $-12$   $^{\circ}\text{C}$  for  $\ln(D_0/a^2)$  of 27.5  $\ln(\text{s}^{-1})$ , 28  $^{\circ}\text{C}$  for  $\ln(D_0/a^2)$  of 19  $\ln(\text{s}^{-1})$ , and  $-53$   $^{\circ}\text{C}$  for  $\ln(D_0/a^2)$  of 39  $\ln(\text{s}^{-1})$ . The weighted average  $T_c$  for these domains would be  $\sim 36$   $^{\circ}\text{C}$ . The Fe-oxide domain inferred to contain 75% of the gas with a  $T_c$  of 51  $^{\circ}\text{C}$  has similar kinetics and  $T_c$  to that of Shuster et al. (2005) ( $E_a$  of 163 kJ/mol;  $T_c$  of  $\sim 51$   $^{\circ}\text{C}$ ) and that of the goethite sample from Reiners et al. (2014;  $E_a$  of 140 kJ/mol;  $T_c$  of 52  $^{\circ}\text{C}$ ).

TABLE 4. HELIUM DIFFUSION EXPERIMENT RESULTS

Step	T* (°C)	T (h)	<sup>3</sup> He (Matom)	(±) (Matom)	<sup>4</sup> He (Matom)	(±) (Matom)	Step age <sup>†</sup> (Ma)	(±) (Ma)
<b>A. Sample 13PRCP8U (Mn-oxide)</b>								
1	120.0	3.0	19.6	1.6	215.5	52.4	0.05	0.01
2	130.0	28.0	18.5	0.8	398.4	36.1	0.51	0.05
3	180.0	2.0	26.6	1.0	1198.6	34.1	1.57	0.08
4	210.0	1.0	53.1	1.5	3997.6	61.7	2.92	0.10
5	240.0	1.0	102.5	1.8	8817.0	71.9	3.40	0.08
6	300.0	1.0	29.6	0.9	2607.5	35.4	3.50	0.12
7	330.0	1.0	2.8	0.3	251.2	44.7	3.54	0.73
8	279.9	2.0	0.1	0.1	8.8	41.0	2.57	12.09
9	200.0	3.0	BDL	BDL	0.3	46.1	BDL	BDL
10	370.0	1.0	3.3	0.4	317.5	33.9	3.89	0.59
11	429.9	1.0	5.1	0.4	506.7	45.7	4.01	0.49
12	419.9	1.0	0.7	0.2	60.9	35.5	3.71	2.34
13	410.0	1.0	0.3	0.1	26.6	34.5	3.59	4.89
14	410.0	1.0	0.2	0.1	27.4	37.2	5.79	8.62
15	449.9	1.0	1.2	0.2	114.5	38.6	3.67	1.39
16	385.0	2.0	0.0	0.1	3.0	34.6	3.67	43.48
17	445.0	1.0	0.7	0.2	53.4	43.8	3.20	2.77
18	500.0	0.5	1.9	0.3	182.8	38.6	3.86	0.98
19	600.0	0.5	3.3	0.3	313.2	38.7	3.79	0.60
20	700.0	0.5	0.4	0.1	44.5	32.1	5.08	4.08
<b>B. 13PRCP8L (Fe-oxide)</b>								
1	120.0	3.0	19.6	0.7	409.4	57.3	1.14	0.16
2	140.0	26.0	11.1	0.6	459.5	38.3	3.27	0.32
3	180.0	2.0	9.6	0.5	364.1	35.2	2.88	0.33
4	210.0	1.0	5.2	0.4	197.4	41.4	2.89	0.65
5	240.0	1.0	8.2	0.4	319.3	36.6	3.02	0.39
6	300.0	1.0	21.0	0.9	853.1	34.8	3.18	0.19
7	330.0	1.0	16.9	0.7	653.9	38.5	2.99	0.22
8	280.0	2.0	3.0	0.3	116.9	39.9	3.08	1.10
9	200.0	3.0	0.1	0.1	9.1	41.2	13.36	63.17
10	369.9	1.0	33.2	1.0	1354.4	50.3	3.20	0.16
11	429.9	1.0	101.2	1.6	4267.2	40.1	3.34	0.08
12	420.0	1.0	26.1	1.0	1057.9	39.7	3.17	0.18
13	410.0	1.0	11.2	0.6	467.5	30.1	3.30	0.28
14	409.9	1.0	7.9	0.5	345.9	37.0	3.49	0.43
15	450.0	1.0	37.0	0.9	1626.1	42.7	3.53	0.14
16	385.0	2.0	3.7	0.3	173.9	40.3	3.79	0.93
17	445.0	1.0	16.6	0.7	769.4	40.4	3.78	0.27
18	499.9	0.5	36.8	1.1	1692.9	70.0	3.74	0.20
19	~800	45.0	27.3	0.8	1345.3	31.7	4.08	0.17

Note: BDL—below detection limit; Matoms = 10<sup>6</sup> atoms; sample mass = 0.13 mg.

\*Temperatures were typically controlled to within ±0.5 °C.

†Calculation of step ages assumes a bulk (U-Th)/He age = 2.73 ± 0.03 Ma, and a <sup>4</sup>He/<sup>3</sup>He production ratio during proton irradiation = 10.

## Ar Analyses

The results of the step-heating analyses are summarized in Table 6. The initial four steps define a range from 1.16 to 3.40 Ma age but are characterized by low radiogenic <sup>40</sup>Ar yields and large uncertainties. Steps 5–10, comprising nearly 90% of the <sup>39</sup>Ar release, define a plateau with an age of 3.60 ± 0.08 Ma (Fig. 9). Isochron treatment of these steps yielded an inverse isochron age of 3.70 ± 0.43 Ma (mean square of weighted deviates [MSWD] = 1.74), which is less precise but statistically identical to the plateau age. The trapped Ar component associated with these steps has an atmospheric composition (<sup>40</sup>Ar/<sup>36</sup>Ar)<sub>trapped</sub> = 287 ± 37. We interpret the 3.6 Ma age to represent either the timing of formation of the Mn-oxides in this vein or, alternatively, the timing of rapid cooling through Ar closure in the Mn-oxides following an earlier period of vein formation.

## DISCUSSION

### Geochemistry Interpretations

Elemental contents of degassed and undegassed aliquots show that presenting data as molar ratios normalized to the summation of Fe and Mn may, in some cases, yield spurious results due to the volatilization of Fe and Mn during He extraction. Compositions of some aliquots suggest that apart from Fe and Mn, some much more volatile elements (e.g., Cu, Ba, Pb, and Zn) are affected by high-temperature laser heating (Fig. 4). Although we saw this elemental loss within high laser heating extraction, we did not observe correlations between these elements and (U-Th)/He age. Because U and Th are less volatile than these elements, this suggests that U and Th volatilization did not occur to a significant degree in most of these samples and did not affect He ages in the majority of the samples. Exceptions are the few high-intensity lasing

samples in Figure 4C showing anomalously high Th/U and old ages.

Two distinct Mn-oxide phases were found in fracture-fill and cement materials across all faults in this study. Because Ba is nearly insoluble in sulfate-bearing solutions, the relatively high Ba (as well as barite) implies either a sulfate-poor fluid or a local Ba source. Corroded feldspar grains seen in some samples provide evidence for a local Ba source from feldspars.

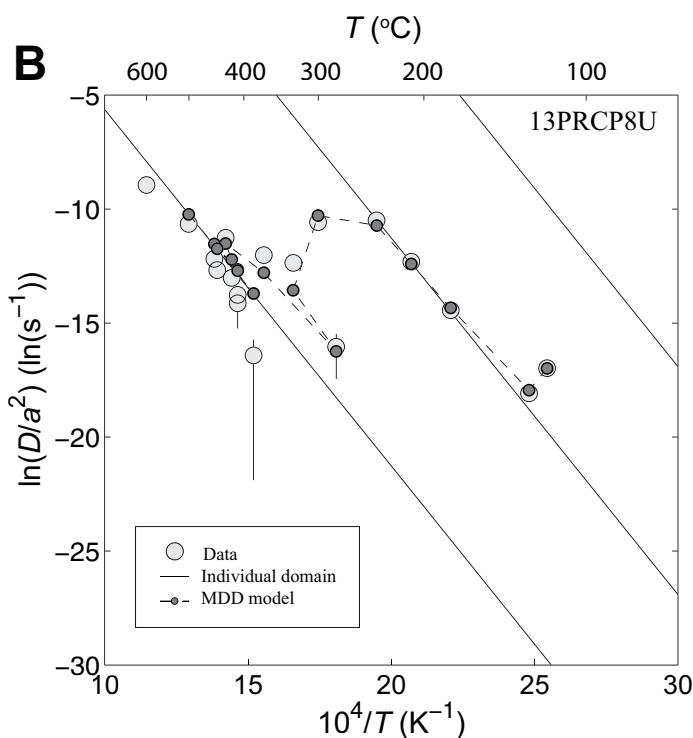
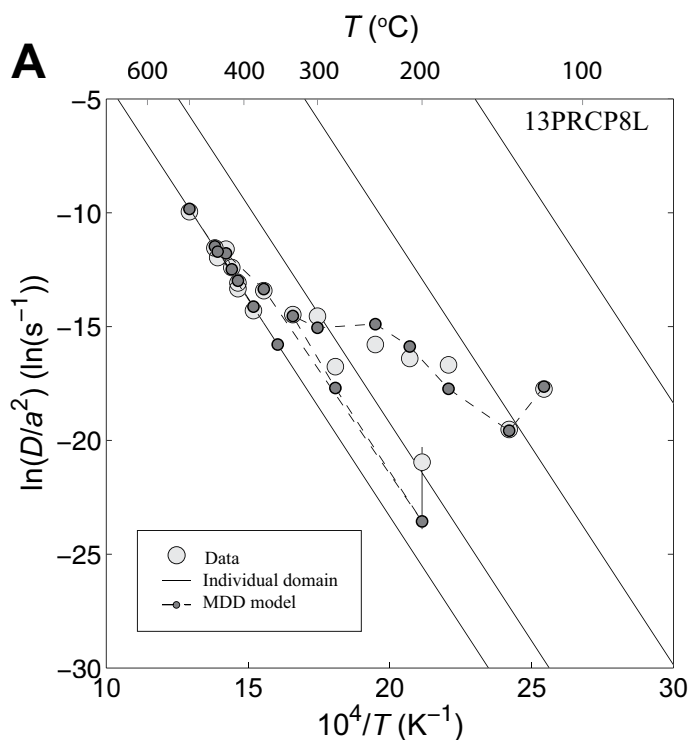
### Age Interpretations

(U-Th)/He ages from the north fault that met reliability criteria (Th/U < 0.01; uncertainty < 5%) were selected to determine weighted mean ages for Fe- and Mn-oxides (3.29 ± 0.03 Ma, 2.73 ± 0.02 Ma, respectively; standard error at 1σ). Uncertainties reported on weighted means are the reciprocal square root of the sum of all individual weights. Figure 8 shows apparent ages at high fractional release plateau into ages around ca. 3.6 Ma. This, combined with concordant <sup>40</sup>Ar/<sup>39</sup>Ar plateau and total gas ages of 3.6 Ma, strongly suggests that these Fe- and Mn-oxides formed at 3.6 Ma.

Although previous <sup>40</sup>Ar/<sup>39</sup>Ar dates by Chan et al. (2001) on oxide cement (mixture of mostly hollandite and some cryptomelane) from the south fault showed a complex age spectrum, their interpreted plateau at ca. 25–20 Ma is much older than any of the dates obtained here. However, we note that ~20% of the gas in the Chan et al. (2001) study was younger than ca. 17 Ma, and ~30%–40% was older than 30 Ma. Our own <sup>40</sup>Ar/<sup>39</sup>Ar date of 3.6 Ma, which was acquired on fracture-fill material from the north fault, is more similar to our relatively young (U-Th)/He dates (as well as those of Reiners et al., 2014) at 3.4–0.50 Ma. All these samples were likely collected within a few tens of meters from each other. Although we cannot rule out the possibility of 25–20 Ma ages in the region, we consider the younger age of 3.6 Ma to be a more likely estimate of the formation ages for these oxide deposits. We tentatively attribute the older Ar dates to possible contamination from detrital K bearing phases.

Reiners et al. (2014) proposed that the discrepancy between the preferred 25–20 Ma <sup>40</sup>Ar/<sup>39</sup>Ar age of Chan et al. (2001) and the 3–2 Ma (U-Th)/He ages in Flat Iron Mesa could be explained if the Ar system recorded initial formation of oxide material, but the He system recorded much later addition of U-Th to oxide material, or its recrystallization, or both, ca. 3–2 Ma. This would require the precursor material to have very low eU (but not K) until 3–2 Ma. According to Reiners et al. (2014), this

**Figure 7.** Arrhenius plots for  $^3\text{He}$  diffusion data on aliquots of Fe- and Mn-oxide fracture-fill material (sample 13PRCP8) plotted assuming spherical diffusion domain geometry. (A) Fe-oxide Arrhenius plot. Circular gray symbols are Fe-oxide data from sample 13PRCP8. Four lines show kinetics for four model domains with  $E_a$  of 159 kJ/mol and  $\ln(D_0/a^2)$  of 15, 27.5, 19, and 39  $\ln(\text{s}^{-1})$ . The dark-gray dots are values of  $D/a^2$  predicted for  $^3\text{He}$  release pattern for the same heating schedule as the actual sample if these four model domains contained the following molar fractions: 0.75, 0.09, 0.09, and 0.07 of the He in the bulk sample. (B) Mn-oxide Arrhenius plot. Circular gray symbols are Mn-oxide data from sample 13PRCP8. Three lines show kinetics for four domains with  $E_a$  of 130 kJ/mol and  $\ln(D_0/a^2)$  of 20, 30, and 10  $\ln(\text{s}^{-1})$ . The dark-gray dots represent the predicted  $^4\text{He}$  release pattern for the same heating schedule as the actual sample if these four domains contained molar fractions 0.86, 0.07, and 0.07 of the He in the bulk sample. MDD—multiple diffusion domain.



addition of U-Th and/or recrystallization might not have fully reset the Ar system, but it did completely reset the He system. This hypothesis may have been a reasonable way to explain the discrepancy between earlier Ar and He dates, but the new ca. 3.6 Ma  $^{40}\text{Ar}/^{39}\text{Ar}$  ages presented here, and their correspondence with the step-age interpretations of He ages (Fig. 8), lead us to a simpler interpretation that all Fe- and Mn-oxide in Flat Iron Mesa formed at ca. 3.6 Ma, and the observed variability between (U-Th)/He ages within aliquots is due to diffusive loss of He within samples.

### He Diffusivity and Fractional Retention

One possible explanation for the variation in (U-Th)/He ages in both the study by Reiners et al. (2014) and this study is diffusive He loss after initial oxide formation at 3.6 Ma. On average, the mean ages of Fe- and Mn-oxides are 3.29 and 2.73 Ma, respectively, would require ~10% and ~25% fractional loss, but some aliquots would have lost significantly more than others. Specifically, Fe-oxides from the north, south, and east faults would have lost 4.7%–21%, 7.9%–32%, and 31%–85%, respectively. Mn-oxides from the north and south faults would have lost 18%–61% and 14%–86%, respectively.

Our diffusion experiments on Fe- and Mn-oxides from the north fault allow us to test this

hypothesis. Apparent  $T_c$  values calculated from multidomain models of the Fe- and Mn-oxide diffusion experiments are 36 °C for Fe-oxide and 17 °C for Mn-oxide. However, a more useful parameter than  $T_c$  for interpreting (U-Th)/He ages in cases where samples may have formed at temperatures near or below  $T_c$  is the fraction

of radiogenic He retained for isothermal holding. Similar to Reiners et al. (2014), we used Equation 5 from Wolf et al. (1998) to calculate fractional He retention as a function of isothermal holding for a duration of 3.6 m.y. at various temperatures using the kinetics measured in our diffusion experiments for Fe- and Mn-oxides.

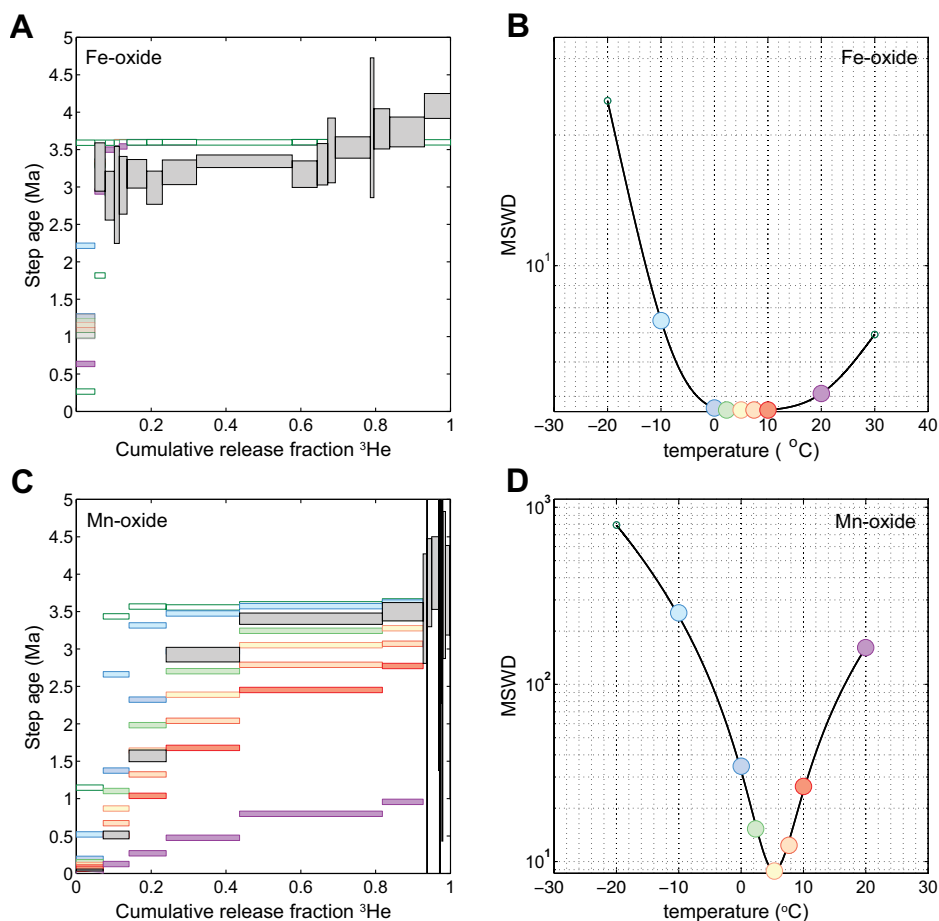


**Figure 8.** Using bulk ages of  $3.29 \pm 0.03$  Ma and  $2.73 \pm 0.02$  Ma for Fe- and Mn-oxide, respectively, and He diffusion parameters, we created step age vs. cumulative  $^3\text{He}$  release fraction plots. (A) Fe-oxide plot shows more consistent  $^3\text{He}$  release patterns in which  $\sim 75\%$  of  $^3\text{He}$  released is ca. 3.6–3.0 Ma. (B) Fe-oxide best-fit effective diffusion temperature solution shows as minima in the mean square of weighted deviates (MSWD) misfit. (C) Mn-oxide plot shows variable  $^3\text{He}$  releases:  $\sim 40\%$  of  $^3\text{He}$  released has ages from 3.0 to 0.5 Ma,  $\sim 50\%$  of  $^3\text{He}$  released has age of 3.6–3.0 Ma, final  $\sim 10\%$  of  $^3\text{He}$  released has a more complicated release pattern from 5 to 0 Ma. (D) Mn-oxide best-fit effective diffusion temperature solution shows as minima in the MSWD misfit.

To do this, we weighted each domain by their inferred proportions from the He diffusion experiments to calculate apparent bulk retention fractions at various temperatures.

Because we do not know the actual temperatures in which these samples formed, nor their subsequent thermal histories, our models provide several end-member possibilities of isothermal holding for 3.6 m.y. and resulting predicted fractional retention (Fig. 10). For holding temperatures, we considered two possibilities: (1) formation at temperatures corresponding to  $\sim 1$ – $2$  km depth and only very recent exhumation, and (2) formation and holding at the surface and surficial temperatures.

Various studies have attempted to constrain Neogene erosional exhumation in the Colorado

Plateau (Pederson et al., 2002; McKeon, 2009; Kelley et al., 2010; Garcia, 2011; Hoffman et al., 2011; Lee et al., 2013; Lazear et al., 2013; Murray et al., 2016). Karlstrom et al. (2012) estimated 0.5–1.5 km of erosional exhumation across the central Colorado Plateau since ca. 20–10 Ma. Lazear et al. (2013) estimated

an average of 0.8–1 km of rock uplift across the northern Colorado Plateau since 10 Ma. Other more local studies, like Hoffman et al. (2011), have estimated 1.2–1.9 km of erosion in the last 10–5 m.y. in the Book Cliffs area ( $\sim 115$  km north of the study area), 2–3 km of erosion since 5–4 Ma in Canyonlands ( $\sim 40$  km southwest of the study area), and 1.5–2 km of erosion since 10–4 Ma at Monument Uplift ( $\sim 200$  km south of the study area). Darling et al. (2012) inferred slow incision rates (0.1 km/m.y.) of the Colorado River near Cataract Canyon ( $\sim 100$  km southwest of the study area). Murray et al. (2016) estimated 1.5–2 km of erosional exhumation during the past 5 m.y., but most likely in the last 3–2 m.y. in the Henry Mountains ( $\sim 120$  km southwest of the study area). Most of these studies have constrained erosion rates between 10 and 4 Ma with varying rates of exhumation ( $\sim 0.5$ – $2$  km). If all of the erosion ( $\sim 0.5$ – $1.5$  km) that occurred in the last 10 m.y. is inferred to have occurred since 3.6 Ma, then our samples could have been held at  $\sim 20$ – $40$  °C until recently. Our other end-member model is that these oxides formed at or near the surface ( $\sim 10$ – $15$  °C;  $\sim 0.5$  km) and experienced little to no erosion in the last 3.6 m.y.

Figures 10A and 10B show the fractional He retention for each modeled domain and the bulk samples as represented in the aliquots used in the diffusion experiments (Table 5) for 3.6 Ma, at varying temperatures. For the surface temperature scenario ( $\sim 10$ – $15$  °C;  $\sim 0.5$  km) and for 3.6 m.y. of holding (implying an erosion rate of 0.15 km/m.y.), Mn-oxide domains would have lost  $\sim 50\%$ – $60\%$  of their He, whereas Fe-oxide domains would have lost  $\sim 10\%$  of their He. This would correspond to (U-Th)/He ages for Mn-oxides of ca. 1.9 Ma and Fe-oxides of ca. 3.2 Ma. If, on the other hand, oxides were held at the most extreme temperature (40 °C;  $\sim 1.5$  km depth) for 3.6 m.y. (implying an erosion rate of 0.42 km/m.y.), Mn-oxide domains would have lost  $\sim 95\%$  of their He, and Fe-oxide domains may have lost  $\sim 15\%$  of their He. This would imply that (U-Th)/He ages for Mn-oxides should be younger than 0.4 Ma, and Fe-oxides should be ca. 3.1 Ma. Taking the observed weighted ages (3.29 Ma for Fe-oxides and 2.73 Ma for Mn-oxides) into consideration, it

TABLE 5. SUMMARY OF MULTIPLE DIFFUSION DOMAIN MODEL PARAMETERS

Sample	$E_a$ (kJ/mol)	$\ln(D_0/a^2)_1$ ( $\ln[s^{-1}]$ )	$\ln(D_0/a^2)_2$ ( $\ln[s^{-1}]$ )	$\ln(D_0/a^2)_3$ ( $\ln[s^{-1}]$ )	$\ln(D_0/a^2)_4$ ( $\ln[s^{-1}]$ )	$F_1$	$F_2$	$F_3$	$F_4$	$T_c$ (°C)
13PRCP8-U										
Mn-oxide	130	20.0	30.0	10.0	–	0.86	0.07	0.07	–	16.5
13PRCP8-L										
Fe-oxide	159	15.0	27.5	19.0	39.0	0.75	0.09	0.09	0.07	36.3

Note: The  $^3\text{He}$  in the Mn-oxide was fitted with a three-domain model; the Fe-oxide was fitted with four domains.  $E_a$ —activation energy;  $F$ —fraction of  $^3\text{He}$  contained within a given model domain;  $T_c$ —closure temperature.



TABLE 6. ARGON STEP-HEATING ANALYSES: SAMPLE 13PRCP8

Incremental heating	Temperature (°C)	<sup>36</sup> Ar [fA]	<sup>37</sup> Ar [fA]	<sup>38</sup> Ar [fA]	<sup>39</sup> Ar [fA]	<sup>40</sup> Ar [fA]	Age (Ma)	±1σ	<sup>40</sup> Ar* (%)	<sup>39</sup> Ar <sub>K</sub> (%)	K/Ca	±1σ
LU2059-001	400						3.402	±1.570	3.573	1.804		
LU2059-002	500	1.543	4.460	0.352	13.553	41.858	3.697	±0.884	8.408	2.926	1.307	±0.143
LU2059-003	550	0.720	3.914	0.125	10.453	10.116	1.159	±1.059	4.537	2.257	1.149	±0.145
LU2059-004	600	0.370	8.113	0.182	14.001	34.714	2.969	±0.737	24.087	3.023	0.742	±0.045
LU2059-005	650	0.483	6.425	0.146	25.039	72.496	3.466	±0.411	33.680	5.406	1.676	±0.139
LU2059-006	725	0.757	9.000	0.088	67.893	219.940	3.878	±0.162	49.553	14.658	3.244	±0.195
LU2059-007	800	1.467	19.042	0.128	159.580	481.008	3.609	±0.084	52.581	34.452	3.604	±0.098
LU2059-008	850	1.355	16.972	0.173	118.423	337.484	3.412	±0.116	45.720	25.567	3.000	±0.093
LU2059-009	900	0.223	3.494	0.042	29.197	98.319	4.031	±0.497	59.815	6.303	3.593	±0.547
LU2059-010	1000	0.171	2.613	0.052	13.536	43.602	3.856	±1.248	46.307	2.922	2.228	±0.443
LU2059-011	1150	0.181	0.689	0.021	2.539	10.883	5.130	±8.896	16.922	0.548	1.585	±1.256
LU2059-012	1300	-0.092	0.694	0.000	0.624	-11.79889712	-22.81	±49.108	30.153	0.135	0.387	±0.269

seems likely that our Fe- and Mn-oxides formed near the surface and experienced very little erosional exhumation (<0.5 km) since formation ca. 3.6 Ma.

We also considered these same temperature ranges for 20 m.y. of isothermal holding. This predicts a much bigger difference in Fe- and Mn-oxide fractional retention. Mn-oxide domains held at surface temperatures (~13 °C) for 20 m.y. would lose ~90% of their He, but Fe-oxide domains would lose ~10%. This corresponds to (U-Th)/He ages for Mn-oxides of 2 Ma and Fe-oxides of 18 Ma. If oxides were held for 20 m.y. at 40 °C, Mn-oxide domains would lose ~95 of their He; however, Fe-oxides would lose ~20% of their He. This would indicate (U-Th)/He ages of 1 Ma and 16 Ma for Mn- and Fe-oxides, respectively. Although we do see Mn-oxide (U-Th)/He ages in this range (2–1 Ma), we do not see Fe-oxide He ages greater than 3.60 Ma, except for a few outliers, but none has ages of 18–16 Ma. This large predicted age difference for the Fe- and Mn-oxides does not support the older <sup>40</sup>Ar/<sup>39</sup>Ar age model of Chan et al. (2001).

The results of these fractional retention models support the interpretation that ~10%–50% of the radiogenic He was lost from some samples, and this is responsible for both the dispersion observed in He ages and the fact that they are younger than the 3.6 Ma <sup>40</sup>Ar/<sup>39</sup>Ar age. The possibility that these oxides may have been exhumed from depths of 0.5–1.5 km in the last 3.6 m.y. seems unlikely. If they did form 0.5–1.5 km (or more) below the surface, He ages for Fe- and Mn-oxides should be much younger, because they would not be able to retain the large amounts of He necessary to match the He ages we observe. For example, if these oxides formed at 2 km depths, which is roughly what some regional studies predict for erosional exhumation depth since ca. 10 Ma, our model shows that Fe- and Mn-oxide ages should be 3.0 Ma and 0.2 Ma, respectively, but what we see are He ages that are older (3.29 Ma for Fe-oxides and 2.73 Ma for Mn-oxides; weighted He ages). Instead, it is more likely that samples

from this study area were formed at shallower depths (<0.5 km) and held at temperatures of ~10–15 °C in order for the oxides to retain enough He to be consistent with our He ages and domain modeling.

A complication with the interpretation of diffusive He loss as the explanation for the dispersion in (U-Th)/He ages is the fact that the observed Mn-oxide ages are 3.0–1.4 Ma (weighted average bulk age is 2.73 ± 0.017 Ma), whereas fractional retention models predict ages of ca. 1.5–0.20 Ma. A similar but less severe discrepancy exists for Fe-oxides: ages are 3.4–2.8 Ma (weighted average bulk age is 3.29 ± 0.028 Ma), and fractional retention models predict ca. 3.3–3.0 Ma. We suggest that this is due to variation in proportions of domains with differing retentivity among aliquots, including those that were analyzed for ages and those used for diffusion experiments. Since each dated aliquot is not a homogeneous sample but a mixture of different phases, we cannot assume that the same proportions of each domain, or even the same types of domains, are present in each aliquot. For example, two texturally and mineralogically different Mn-oxide phases were dated from sample 14VGCP10, 14VGCP10\_MnL (Ba-rich Mn-oxide phase) with (U-Th)/He ages

of 2.8–1.9 Ma and 14VGCP10\_MnC (relatively pure Mn-oxide phase) with (U-Th)/He ages of 1.9–1.4 Ma. SEM imaging of representative grains of both phases revealed that different proportions of each phase were present within dated aliquots, resulting in the variable range in ages observed.

Assuming the weighted average bulk age for Fe- and Mn-oxides of 3.29 Ma and 2.73 Ma, respectively, we can calculate the proportions of each domain that would be required to predict these bulk He ages for 3.6 m.y. of isothermal holding at 10–15 °C. This corresponds to expected He retention of ~90% for Fe-oxides, which is observed, and expected He retention of ~75% for Mn-oxides (dated Mn-oxide aliquots retain ~45% of He). This hypothetical domain distribution for Mn-oxide requires a greater fraction of He in one of the more retentive domains. No unique solution exists for this, but one is a distribution with the following proportions: ln(*D<sub>0</sub>/a<sup>2</sup>*) of 20 with 20% of He, ln(*D<sub>0</sub>/a<sup>2</sup>*) of 30 with 15% of He, and ln(*D<sub>0</sub>/a<sup>2</sup>*) of 10 with 65% of He (Fig. 10C). Based on these models and the variability of domain proportions within oxide aliquots, it is not possible to select truly representative samples, unless dating is done on the same specimen used for

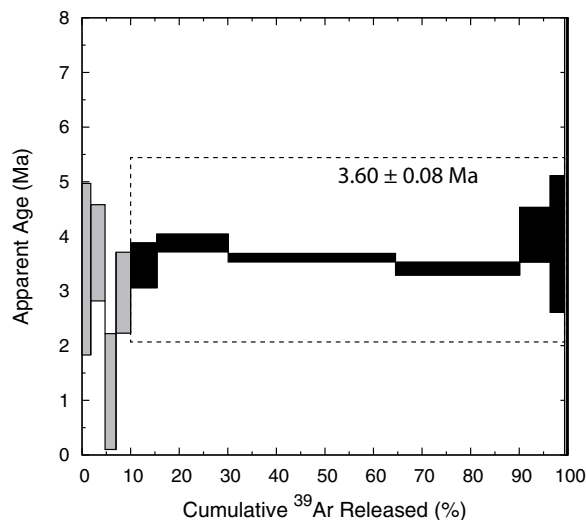
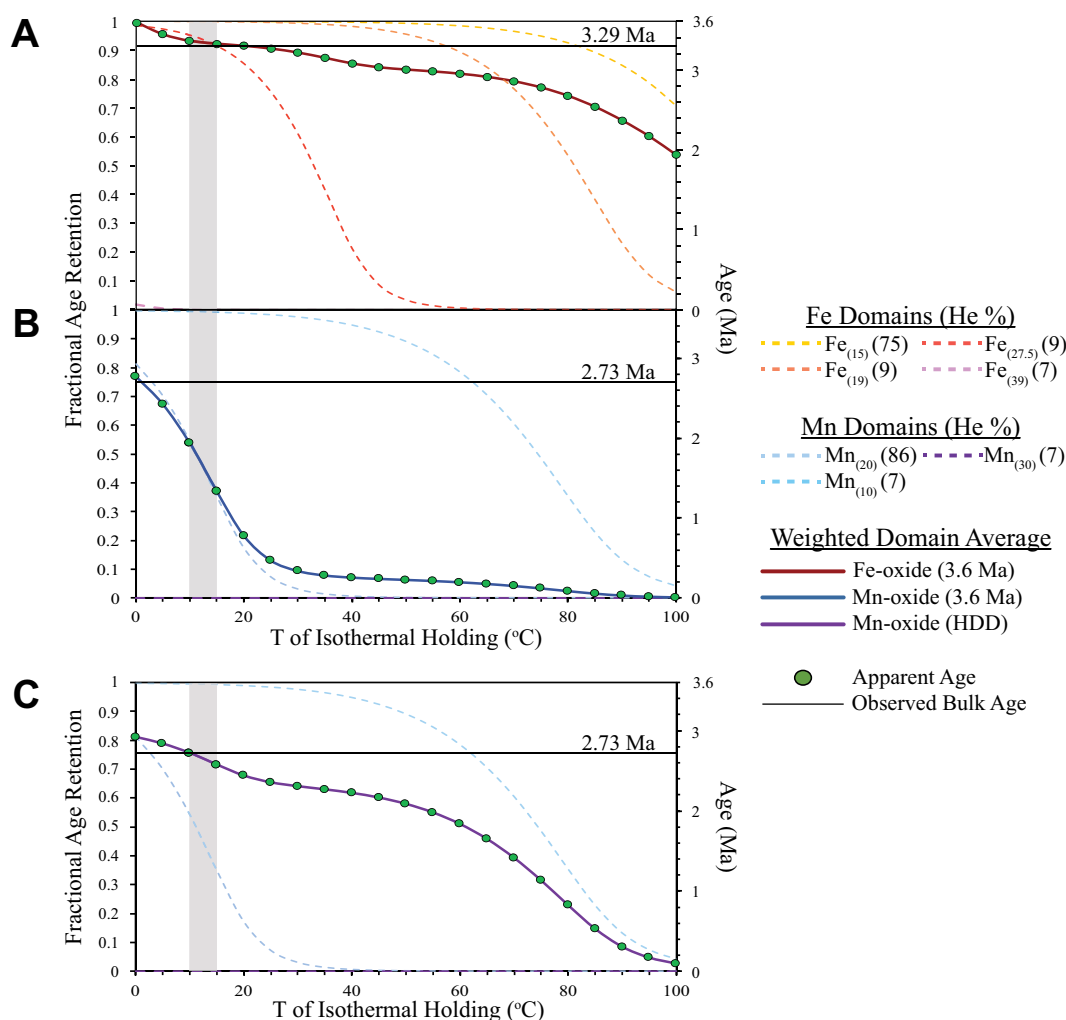


Figure 9. <sup>40</sup>Ar/<sup>39</sup>Ar age spectra of Mn-oxide fracture-fill material sample 13PRCP8.



**Figure 10.** Fractional retention models for Fe- and Mn-oxides, based on Wolf et al. (1998), for isothermal holding for 3.6 m.y. Bulk age calculations predict Fe- and Mn-oxide fractional He retention of 90% and 75%, respectively. Vertical gray bars refer to likely temperatures experienced by oxides in this study. Trend lines represent predictions for oxides based on He diffusion experiments on sample 13PRCP8. See Table 6 for model parameters. Light dashed lines represent different domain sizes and associated percent of He in each domain, e.g., Fe<sub>(15)</sub>(75) refers to  $\ln(D_0/a^2)$  of 15 with 75% of He within this domain. Green circles on weighted domain average trends (solid lines) refer to apparent age at the associated temperature. (A) Fe-oxide fractional retention model showing Fe-oxide as the most retentive phase at 10–15 °C, retaining ~92% of its He. (B) Mn-oxide fractional retention model showing that at 10–15 °C, Mn-oxide retains ~45% of its He. (C) Hypothetical domain distribution (HDD) model for Mn-oxide that would retain ~75% of its He at 10–15 °C.

the diffusion experiment. This was not done in this case due to worries of volatilizing U and Th in the final degassing step, but procedures could be developed to avoid this and measure both ages and diffusion kinetics on the same aliquots.

#### <sup>4</sup>He/<sup>3</sup>He Thermochronometry

Using the MDD (multiple diffusion domain) model parameters in Table 5, we conducted forward calculations of simultaneous production and outward diffusion (numerical method of Shuster and Cassata, 2015) of radiogenic <sup>4</sup>He from each spherical diffusion domain held at isothermal conditions for a 3.6 m.y. duration. Results of these radiogenic <sup>4</sup>He calculations were then passed through a model laboratory degassing, assuming a spatially uniform distribution of <sup>3</sup>He, and using the same heating schedule as the analyses. By summing results of the domains, model results could be directly com-

pared with the <sup>4</sup>He/<sup>3</sup>He release spectra shown in Figure 8. Models for both the Mn-oxide and Fe-oxide were calculated between –20 °C and +30 °C; the best-fitting temperatures for each sample were identified at the minimum misfit between models and data and corresponded to the effective diffusion temperatures (EDT; Tremblay et al., 2014a,b) that best predicted each data set. We found that the age discordance of each sample can be explained solely by diffusive loss of <sup>4</sup>He at near-surface temperatures since the samples precipitated at ca. 3.6 Ma. We also found internally consistent EDTs of  $4.5 \pm 15$  °C (Fe-oxide) and  $5.3 \pm 4$  °C (Mn-oxide) for the two samples (Fig. 8), which are lower than but not extremely different from estimated near-surface mean annual temperatures (MATs, which will be slightly lower than the EDTs; Tremblay et al., 2014a,b) averaged over the last 3.6 m.y. at this site. The MAT at Moab, Utah, is 14 °C, but the MAT at our study area is likely ~3 °C lower than Moab due to elevation

difference (assuming a lapse rate ~6 °C/km). Even then, the MAT of the study area is higher than the predicted EDT, which may be consistent with a lower MAT when averaged over the glacial-interglacial cycles of the last few million years.

#### Implications

The preceding discussion leads us to favor a scenario involving the formation of all secondary Fe- and Mn-oxides, both fracture-fill and cement material, from Flat Iron Mesa at 3.6 Ma. Although we cannot rule out the possibility of more recent formation of some samples in this region, diffusive loss of He is the likely culprit for variability among He dated aliquots and the fact that most samples have He ages younger than the <sup>40</sup>Ar/<sup>39</sup>Ar age of 3.6 Ma. Precipitation of oxides near these faults at this time may reflect changes in groundwater flux or chemistry, which could in turn reflect regional

tectonic or geomorphic changes, or global climate changes. Regionally, Murray et al. (2016) proposed a major increase in erosion rates (1.5–2 km) in the area surrounding the Henry Mountains (~120 km from this study area) in the last 5 m.y., and likely more recently in the last 2–3 m.y. Such a transient pulse of rapid erosion could conceivably incise to ~1 km depths and rearrange shallow groundwater circulation patterns at local scales. Although previous regional studies (Pederson et al., 2002; McKeon, 2009; Hoffman et al., 2011; Karlstrom et al., 2012; Lazear et al., 2013) inferred erosional exhumation rates to vary from 0.5 to 3 km from 2 to 10 Ma, our data and interpretations suggest that, at least locally, erosional exhumation rates have been significantly slower since at least 3.6 m.y. This may be because of local effects related to varying rates of knickpoint propagation on Colorado River tributaries, or more widespread decreases in erosion since 3.6 Ma.

At a much broader scale, Riffel et al. (2016) found a very similar range in (U-Th)/He ages (3.6–0.4 Ma) on pedogenic goethite from the Parana flood basalt in Brazil. A review of literature on other pedogenic weathering deposits did not reveal an exact match to our formation age, but we note that 4–2 Ma is similar to the age of important changes occurring climatologically around the world, including abrupt terrestrial climate changes worldwide at ca. 2.4 Ma (e.g., Kukla, 1989), shoaling of the equatorial Pacific thermocline at ca. 3.7 Ma as a result of closure of the Panamanian seaway (Zhang et al., 2012), inferred onset of Northern Hemisphere glaciation at 2.67 Ma (e.g., Prueher and Rea, 1998), interglacial intensification of the North Atlantic at 2.95–2.82 Ma (Bartoli et al., 2005), barred intermediate-water circulation through the Panama Strait at 4.5–4.0 Ma with short-lasting re-openings near 3.8 and 3.4–3.3 Ma (Haug et al., 2005; Steph, 2005), glaciation to midlatitudes at 2.64 Ma (Bailey et al., 2013), initial advances of the Laurentide ice sheet at 2.47 Ma (Rovey and Balco, 2010), and initial phases of intermountain basin erosion accompanying widespread alpine glaciation in the Rockies at 2.6 Ma (Reiners et al., 2011).

If our interpretations of (U-Th)/He ages of oxide material in this study area are correct, then He dating of secondary oxides may reveal formation ages if He diffusion kinematics are understood and corrected for. These ages in turn likely reflect events associated with changes in groundwater flux, fault movement, or both. Formation of these oxides at this time could reflect a major regional hydrologic change such as increased flux of groundwater discharge due to increased precipitation or a more local effect related to fault activity.

## CONCLUSIONS

(U-Th)/He ages on secondary fracture-fill and cement material of Fe- and Mn-oxides from the Navajo Sandstone at Flat Iron Mesa, Utah, range from ca. 3.43 to 0.50 Ma, and new  $^{40}\text{Ar}/^{39}\text{Ar}$  dates from the same material are 3.6 Ma, consistent with the oldest (U-Th)/He ages. The (U-Th)/He ages of samples from three different fault zones have distinct (U-Th)/He age and compositional relationships: Fe- and Mn-oxide fracture-fill material from the north fault has (U-Th)/He ages from 3.43 to 2.84 Ma (bulk age =  $3.29 \pm 0.028$  Ma) and from 2.93 to 1.39 Ma (bulk age =  $2.73 \pm 0.017$  Ma), respectively, i.e., much younger than previous 25–20 Ma  $^{40}\text{Ar}/^{39}\text{Ar}$  ages from the same area. Ba-rich Mn-oxide phase aliquots have a bulk age of  $2.16 \pm 0.015$  Ma, whereas relatively pure phase Mn-oxides have a younger bulk age of  $1.61 \pm 0.011$  Ma. Fe- and Mn-oxide cement material from the south fault ranges from 3.16 to 0.50 Ma. Botryoidal Fe-oxide from the east fault ranges from 2.47 to 0.55 Ma. Taken together and combined with  $^{40}\text{Ar}/^{39}\text{Ar}$  data, step-heating diffusion experiments on samples of Fe- and Mn-oxide fracture-fill material from the north fault, and fractional retention models, we conclude that oxides in Flat Iron Mesa formed at 3.6 Ma, and the range in ages most likely reflects multidomain diffusive He loss and varying domain proportions between He dated aliquots. We propose that oxides in Flat Iron Mesa formed at or near the surface (<0.5 km) at 3.6 Ma due to hydrologic changes, fault activity, or both, and have experienced very little cooling since formation. Our data and interpretations suggest that erosional exhumation rates over ~1–4 m.y. time scales may be spatially variable in the central Colorado Plateau, possibly driven by local geomorphic effects, and they are not spatially uniform over large regions. The results presented here confirm that secondary oxides are suitable targets for (U-Th)/He thermochronology, but they also illustrate the need for understanding He diffusion kinematics within samples.

## ACKNOWLEDGMENTS

We appreciate helpful reviews from Joel Pederson and Bruce H. Shyu, and editorial handling by Brad Singer. We acknowledge support from National Science Foundation grants EAR-1219653 and EAR-1419745 to Reiners, and support from a Spencer Titley Scholarship and GDL Foundation Scholarship to Garcia. We are thankful for analytical assistance from Uttam Chowdhury and Erin Abel. Garcia thanks Stuart Thomson for providing a digital elevation model of our study area. We also appreciate helpful discussions, comments, and reviews from Mark Barton and Eric Seedorff.

## REFERENCES CITED

- Bailey, I., Hole, G.M., Foster, G.L., Wilson, P.A., Storey, C.D., Trueman, C.N., and Raymo, M.E., 2013, An alternative suggestion for the Pliocene onset of major Northern Hemisphere glaciation based on the geochemical provenance of North Atlantic Ocean ice-rafted debris: *Quaternary Science Reviews*, v. 75, p. 181–194, doi:10.1016/j.quascirev.2013.06.004.
- Baker, A.A., Duncan, D.C., and Hunt, C.B., 1952, Manganese Deposits of Southeastern Utah: U.S. Geological Survey Bulletin 979-B, 157 p.
- Barbeau, D.L., 2003, A flexural model for the Paradox Basin: Implications for the tectonics of the Ancestral Rocky Mountains: *Basin Research*, v. 15, p. 97–115, doi:10.1046/j.1365-2117.2003.00194.x.
- Bartoli, G., Sarnthein, M., Weinelt, M., Erlenkeuser, H., Garbe-Schönberg, D., and Lea, D.W., 2005, Final closure of Panama and the onset of Northern Hemisphere glaciation: *Earth and Planetary Science Letters*, v. 237, p. 33–44, doi:10.1016/j.epsl.2005.06.020.
- Basta, E.Z., and Saleeb, G.S., 1971, Elba manganese ore and their origin, South Eastern Desert, Egypt: *Mineralogical Magazine*, v. 38, p. 235–244, doi:10.1180/minmag.1971.038.294.13.
- Beitler, B., Chan, M.A., and Parry, W.T., 2003, Bleaching of Jurassic Navajo Sandstone on Colorado Plateau Laramide highs: Evidence of exhumed hydrocarbon supergiants?: *Geology*, v. 31, p. 1041–1044, doi:10.1130/G19794.1.
- Beitler, B., Parry, W.T., and Chan, M.A., 2005, Fingerprints of fluid flow: Chemical diagenetic history of the Jurassic Navajo Sandstone, southern Utah, U.S.A.: *Journal of Sedimentary Research*, v. 75, p. 547–561, doi:10.2110/jsr.2005.045.
- Berg, S.S., and Skar, T., 2005, Controls on damage zone asymmetry of a normal fault zone: Outcrop analyses of a segment of the Moab fault, SE Utah: *Journal of Structural Geology*, v. 27, p. 1803–1822, doi:10.1016/j.jsg.2005.04.012.
- Busigny, V., and Dauphas, N., 2007, Tracing paleofluid circulations using iron isotopes: A study of hematite and goethite concretions from the Navajo Sandstone (Utah, USA): *Earth and Planetary Science Letters*, v. 254, p. 272–287, doi:10.1016/j.epsl.2006.11.038.
- Chan, M.A., Parry, W.T., and Bowman, J.R., 2000, Diagenetic hematite and manganese oxides and fault-related fluid flow in Jurassic sandstones, southeastern Utah: *American Association of Petroleum Geologists Bulletin*, v. 84, p. 1281–1310.
- Chan, M.A., Parry, W.T., Petersen, E.U., and Hall, C.M., 2001,  $^{40}\text{Ar}/^{39}\text{Ar}$  age and chemistry of manganese mineralization in the Moab and Lisbon fault systems, southeastern Utah: *Geology*, v. 29, p. 331–334, doi:10.1130/0091-7613(2001)029<0331:AAAACO>2.0.CO;2.
- Chan, M.A., Beitler, B., Parry, W.T., Ormö, J., and Komatsu, G., 2004, A possible terrestrial analogue for haematite concretions on Mars: *Nature*, v. 429, p. 731–734, doi:10.1038/nature02600.
- Chan, M.A., Beitler Bowen, B., Parry, W.T., Ormö, J., and Komatsu, G., 2005, Red rock and red planet diagenesis: Comparisons of Earth and Mars concretions: *GSA Today*, v. 15, no. 8, p. 4–10, doi:10.1130/1052-5173(2005)15[4:RRARPD]2.0.CO;2.
- Chan, M.A., Johnson, C.M., Beard, B.L., Bowman, J.R., and Parry, W.T., 2006, Iron isotopes constrain the pathways and formation mechanisms of terrestrial oxide concretions: A tool for tracing iron cycling on Mars?: *Geosphere*, v. 2, p. 324–332, doi:10.1130/GES00051.1.
- Chan, M.A., Ormö, J., Park, A.J., Stich, M., Souza-Egipsy, V., and Komatsu, G., 2007, Models of iron oxide concretion formation: Field, numerical, and laboratory comparisons: *Geofluids*, v. 7, p. 356–368, doi:10.1111/j.1468-8123.2007.00187.x.
- Chan, M.A., Potter, S.L., Bowen, B.B., Petersen, E.U., Parry, W.T., Bowman, J.R., Barge, L., and Seiler, W., 2012, Characteristics of terrestrial ferric oxide concretions and implications for Mars, in Grotzinger, J., and Milliken, R., eds., *Sedimentary Geology of Mars: Society for Sedimentary Geology Special Pub-*

- lication 102, p. 253–270, doi:10.2110/pec.12.102.0253.
- Danišik, M., Evans, N.J., Ramanidou, E.R., McDonald, B.J., Mayers, C., and McInnes, B.I.A., 2013, (U-Th)/He chronology of the Robe River channel iron deposits, Hamersley Province, Western Australia: *Chemical Geology*, v. 354, p. 150–162, doi:10.1016/j.chemgeo.2013.06.012.
- Darling, A.L., Karlstrom, K.E., Granger, D.E., Aslan, A., Kirby, E., Ouimet, W.B., Lazear, G.D., Coblenz, D.D., and Cole, R.D., 2012, New incision rates along the Colorado River system based on cosmogenic burial dating of terraces: Implications for regional controls on Quaternary incision: *Geosphere*, v. 8, no. 5, p. 1020–1041, doi:10.1130/GES00724.1.
- Doelling, H.H., Oviatt, C.G., and Huntoon, P.W., 1988, Salt Deformation in the Paradox Region: Utah Geological and Mineral Survey Bulletin 122, 93 p.
- Evenson, N.S., Reiners, P.W., Spencer, J.E., and Shuster, D.L., 2014, Hematite and Mn oxide (U-Th)/He dates from the Buckskin-Rawhide detachment system, western Arizona: Gaining insights into hematite (U-Th)/He systematics: *American Journal of Science*, v. 314, p. 1373–1435, doi:10.2475/10.2014.01.
- Farley, K.A., and Flowers, R.M., 2012, (U-Th)/Ne and multi-domain (U-Th)/He systematics of a hydrothermal hematite from eastern Grand Canyon: *Earth and Planetary Science Letters*, v. 359, p. 131–140, doi:10.1016/j.epsl.2012.10.010.
- Farley, K.A., and McKeon, R., 2015, Radiometric dating and temperature history of banded iron formation-associated hematite, Gogebic iron range, Michigan, USA: *Geology*, v. 43, no. 12, p. 1083–1086, doi:10.1130/G37190.1.
- Fechtig, H., and Kalbitzer, S., 1966, The diffusion of argon in potassium-bearing solids, in Schaeffer, A., and Zahlinger, J., eds., *Potassium Argon Dating*: Berlin, Springer, p. 68–107, doi:10.1007/978-3-642-87895-4\_4.
- Foxford, K.A., Garden, I.R., Guscott, S.C., Burley, S.D., Lewis, J.J.M., Walsh, J.J., and Watterson, J., 1996, The field geology of the Moab fault: Utah Geological Association Guidebook, v. 25, p. 265–285.
- Foxford, K.A., Walsh, J.J., Watterson, J., Garden, I.R., Guscott, S.C., and Burley, S.D., 1998, Structure and content of the Moab fault zone, Utah, USA, and its implications for fault seal prediction, in Jones, G., Fisher, Q.J., and Knipe, R.J., eds., *Faulting, Fault Sealing and Fluid Flow in Hydrocarbon Reservoirs*: Geological Society, London, Special Publication 147, p. 87–103, doi:10.1144/GSL.SP.1998.147.01.06.
- Frery, E., Gratier, J.-P., Ellouz-Zimmerman, N., Loiselet, C., Braun, J., Deschamps, P., Blamart, D., Hamelin, B., and Swennen, R., 2015, Evolution of fault permeability during episodic fluid circulation: Evidence for the effects of fluid-rock interactions from travertine studies (Utah–USA): *Tectonophysics*, v. 651–652, p. 121–137, doi:10.1016/j.tecto.2015.03.018.
- Garcia, R., 2011, Cenozoic Intrusive and Exhumation History of the West Elk Mountains, Southwestern Colorado [M.S. thesis]: Socorro, New Mexico Institute of Mining and Technology, 200 p.
- Garrels, R.M., and Christ, C.L., 1965, *Minerals, Solutions, and Equilibria*: New York, Harper & Rowe, 450 p.
- Haug, G.H., Ganopolski, A., Sigman, D.M., Rosell-Mele, A., Swann, G.E.A., Tiedemann, R., Jaccard, S.L., Bollmann, J., Maslin, M.A., Leng, M.J., and Eglinton, G., 2005, North Pacific seasonality and the glaciation of North America 2.7 million years ago: *Nature*, v. 433, p. 821–825.
- Heim, J.A., Vasconcelos, P.M., Shuster, D.L., Farley, K.A., and Broadbent, G., 2006, Dating paleochannel iron ore by (U-Th)/He analysis of supergene goethite, Hamersley Province, Australia: *Geology*, v. 34, p. 173–176, doi:10.1130/G22003.1.
- Hoffman, M., Stockli, D.F., Kelley, S.A., Pederson, J., and Lee, J., 2011, Mio-Pliocene erosional exhumation of the central Colorado Plateau, eastern Utah—New insights from apatite (U-Th)/He thermochronometry, in Beard, L.S., Karlstrom, K.E., Young, R.E., and Billingsley, G.H., eds., *CREvolution 2—Origin and Evolution of the Colorado River System*, Workshop Abstracts: U.S. Geological Survey Open-File Report 2011-1210, p. 132–136.
- Jochems, A.P., and Pederson, J.L., 2015, Active salt deformation and rapid, transient incision along the Colorado River near Moab, Utah: *Journal of Geophysical Research—Earth Surface*, v. 120, no. 4, p. 730–744.
- Karlstrom, K.E., Coblenz, D., Dueker, K., Ouimet, W., Kirby, E., Van Wijk, J., Schmandt, B., Kelley, S., Lazear, G., Crossey, L.J., Crow, R., Aslan, A., Darling, A., Aster, R., et al., 2012, Mantle-driven dynamic uplift of the Rocky Mountains and Colorado Plateau and its surface response: Toward a unified hypothesis: *Lithosphere*, v. 4, p. 3–22, doi:10.1130/L150.1.
- Kelley, S.A., Karlstrom, K.E., Stockli, D., McKeon, R., Hoffman, M., Lee, J., Pederson, J., Garcia, R., and Coblenz, D., 2010, A summary and evaluation of thermochronologic constraints on the exhumation history of the Colorado Plateau—Rocky Mountain region, in Beard, L.S., Karlstrom, K.E., Young, R.E., and Billingsley, G.H., eds., *CREvolution 2—Origin and Evolution of the Colorado River System*, Workshop Abstracts: U.S. Geological Survey Open-File Report 2011-1210, p. 160–167 <http://pubs.usgs.gov/of/2011/1210/>.
- Kettler, R.M., Loope, D.B., and Weber, K.A., 2011, Follow the water: Connecting a CO<sub>2</sub> reservoir and bleached sandstone to iron-rich concretions in the Navajo Sandstone of south-central Utah, USA [Reply]: *Geology*, v. 39, p. e251–e252, doi:10.1130/G32550Y.1.
- Koppers, A.A.P., 2002, ArArCALC—software for <sup>40</sup>Ar/<sup>39</sup>Ar age calculations: *Computers & Geosciences*, v. 28, p. 605–619, doi:10.1016/S0098-3004(01)00095-4.
- Kukla, G., 1989, Long continental records of climate—An introduction: *Palaeogeography, Palaeoclimatology, Palaeoecology*, v. 72, p. 1–9, doi:10.1016/0031-0182(89)90128-4.
- Lanza, N.L., Fischer, W.W., Wiens, R.C., Grotzinger, J., Ollila, A.M., Cousin, A., Anderson, R.B., Clark, B.C., Gellert, R., Mangold, N., Maurice, S., Le Mouélic, S., Nachon, M., Schmidt, M., et al., 2014, High manganese concentrations in rocks at Gale crater, Mars: *Geophysical Research Letters*, v. 41, p. 5755–5763, doi:10.1002/2014GL060329.
- Lazear, G., Karlstrom, K.E., Aslan, A., and Kelly, S., 2013, Denudation and flexural isostatic response of the Colorado Plateau and southern Rocky Mountain region since 10 Ma: *Geosphere*, v. 9, no. 4, p. 792–814, doi:10.1130/GES00836.1.
- Laznicka, P., 1992, Manganese deposits in the global lithogenic system: Quantitative approach: *Ore Geology Reviews*, v. 7, p. 279–356, doi:10.1016/0169-1368(92)90013-B.
- Leal, P.R., 2010, Mineralogy and geochemistry of an epithermal manganese district, Sierras Pampeanas, Argentina: *International Geology Review*, v. 46, no. 1, p. 75–90, doi:10.2747/0020-6814.46.1.75.
- Leal, P.R., Correa, M.J., Ametrano, S.J., Etcheverry, R.O., and de Brodtkorb, M.K., 2008, The manganese deposits of the Pampean Ranges, Argentina: *Canadian Mineralogist*, v. 46, p. 1215–1233, doi:10.3749/canmin.46.5.1215.
- Lee, J.P., Stockli, D.F., Kelley, S.A., Pederson, J.L., Karlstrom, K.E., and Ehlers, T.A., 2013, New thermochronometric constraints on the Tertiary landscape evolution of central and eastern Grand Canyon, Arizona: *Geosphere*, v. 9, no. 2, p. 216–228, doi:10.1130/GES00842.1.
- Levandowski, D.W., Kaley, M.E., Silverman, S.R., and Smalley, R.G., 1973, Cementation in Lyons sandstone and its role in oil accumulation, Denver Basin, Colorado: *American Association of Petroleum Geologists Bulletin*, v. 57, p. 2217–2244.
- Li, J., Vasconcelos, P.M., and Zhang, J., 2002, Behavior of argon gas release from manganese oxide minerals as revealed by <sup>40</sup>Ar/<sup>39</sup>Ar laser incremental heating analysis: *Chinese Science Bulletin*, v. 47, p. 1502–1510, doi:10.1360/02tb9331.
- Lippolt, H.J., and Hautmann, S., 1995, <sup>40</sup>Ar/<sup>39</sup>Ar ages of Precambrian manganese ore minerals from Sweden, India and Morocco: *Mineralium Deposita*, v. 30, p. 246–256, doi:10.1007/BF00196360.
- Lippolt, H.J., Wernicke, R.S., and Bahr, R., 1995, Paragenetic specularite and adularia (Elba, Italy): Concor-
- dant (U+Th)-He and K-Ar ages: *Earth and Planetary Science Letters*, v. 132, no. 1–4, p. 43–51, doi:10.1016/0012-821X(95)00046-F.
- Loope, D.B., and Kettler, R.M., 2015, The footprints of ancient CO<sub>2</sub>-driven flow systems: Ferrous carbonate concretions below bleached sandstone: *Geosphere*, v. 11, no. 3, p. 943–957, doi:10.1130/GES01094.1.
- Loope, D.B., Kettler, R.M., and Weber, K.A., 2010, Follow the water: Connecting a CO<sub>2</sub> reservoir and bleached sandstone to iron-rich concretions in the Navajo Sandstone of south-central Utah, USA: *Geology*, v. 38, p. 999–1002, doi:10.1130/G31213.1.
- Loope, D.B., Kettler, R.M., and Weber, K.A., 2011, Morphologic clues to the origins of iron oxide-cemented spheruloids, boxworks, and pipeline concretions, Navajo Sandstone of south-central Utah, U.S.A.: *The Journal of Geology*, v. 119, p. 505–520, doi:10.1086/661110.
- McKeon, R.E., 2009, The Interaction Between Tectonics, Topography, and Climate in the San Juan Mountains, Southwestern Colorado [M.S. thesis]: Bozeman, Montana, Montana State University, 77 p.
- Murray, K.E., Reiners, P.W., and Thompson, S.N., 2016, Rapid Pliocene–Pleistocene erosion of the central Colorado Plateau documented by apatite thermochronology from the Henry Mountains: *Geology*, v. 44, no. 6, p. 483–486, doi:10.1130/G37733.1.
- Ostwald, J., 1981, Evidence for a biogeochemical origin of the Groote Eylandt manganese ores: *Economic Geology and the Bulletin of the Society of Economic Geologists*, v. 76, p. 556–567, doi:10.2113/gsecongeo.76.3.556.
- Pederson, J.L., Mackley, R.D., and Eddleman, J.L., 2002, Colorado Plateau uplift and erosion evaluated using GIS: *GSA Today*, v. 12, p. 4–10, doi:10.1130/1052-5173(2002)012<0004:CPUAEE>2.0.CO;2.
- Peterson, J.A., 1989, *Geology and Petroleum Resources, Paradox Basin Province*: U.S. Geological Survey Open-File Report 88-440-U, 69 p.
- Pevear, D.R., Vrolijk, P.J., and Longstaffe, F.J., 1997, Timing of Moab fault displacement and fluid movement integrated with burial history using radiogenic and stable isotopes: *Geofluids II*, v. 97, p. 42–45.
- Potter, S.L., and Chan, M.A., 2011, Joint controlled fluid flow patterns and iron mass transfer in Jurassic Navajo Sandstone, southern Utah, USA: *Geofluids*, v. 11, p. 184–198, doi:10.1111/j.1468-8123.2011.00329.x.
- Potter, S.L., Chan, M.A., Petersen, E.U., Dyar, M.D., and Sklute, E., 2011, Characterization of Navajo Sandstone concretions: Mars comparison and criteria for distinguishing diagenetic origins: *Earth and Planetary Science Letters*, v. 301, p. 444–456, doi:10.1016/j.epsl.2010.11.027.
- Prueher, L.M., and Rea, D.K., 1998, Rapid onset of glacial conditions in the subarctic North Pacific region at 2.67 Ma: Clues to causality: *Geology*, v. 26, no. 11, p. 1027–1030, doi:10.1130/0091-7613(1998)026<1027:ROOGCI>2.3.CO;2.
- Reiners, P.W., 2005, Zircon (U-Th)/He thermochronometry: Reviews in Mineralogy and Geochemistry, v. 58, no. 1, p. 151–179, doi:10.2138/rmg.2005.58.6.
- Reiners, P.W., Riihimaki, C.A., and Heffern, E.L., 2011, Clinker geochronology, the first glacial maximum, and landscape evolution in the northern Rockies: *GSA Today*, v. 21, no. 7, p. 4–9, doi:10.1130/G107A.1.
- Reiners, P.W., Chan, M.A., and Evenson, N.S., 2014, (U-Th)/He geochronology and chemical compositions of diagenetic cement, concretions, and fracture-filling oxide minerals in Mesozoic sandstones of the Colorado Plateau: *Geological Society of America Bulletin*, v. 126, p. 1363–1383, doi:10.1130/B30983.1.
- Renne, P.R., Swisher, C.C., Deino, A.L., Karner, D.B., Owens, T.L., and DePaolo, D.J., 1998, Intercalibration of standards, absolute ages and uncertainties in Ar-40/Ar-39 dating: *Chemical Geology*, v. 145, no. 1–2, p. 117–152, doi:10.1016/S0009-2541(97)00159-9.
- Riffel, S.B., Vasconcelos, P.M., Carmo, I.O., and Farley, K.A., 2016, Goethite (U-Th)/He geochronology and precipitation mechanisms during weathering of basalts: *Chemical Geology*, v. 446, p. 18–32, doi:10.1016/j.chemgeo.2016.03.033.
- Rovey, C.W., and Balco, G., 2010, Periglacial climate at the 2.5 Ma onset of Northern Hemisphere glaciation

- inferred from the Whippoorwill Formation, northern Missouri, USA: *Quaternary Research*, v. 73, no. 1, p. 151–161, doi:10.1016/j.yqres.2009.09.002.
- Segal, D.B., Ruth, M.D., and Merin, I.S., 1986, Remote detection of anomalous mineralogy associated with hydrocarbon production, Lisbon Valley, Utah: *The Mountain Geologist*, v. 23, p. 51–62.
- Shuster, D.L. and Cassata, W.S., 2015, Paleotemperatures at the lunar surfaces from open system behavior of cosmogenic  $^{39}\text{Ar}$  and radiogenic  $^{40}\text{Ar}$ : *Geochimica et Cosmochimica Acta*, v. 155, p. 154–171.
- Shuster, D.L., and Farley, K.A., 2004,  $^4\text{He}/^3\text{He}$  thermochronometry: Earth and Planetary Science Letters, v. 217, no. 1–2, p. 1–17, doi:10.1016/S0012-821X(03)00595-8.
- Shuster, D.L., and Farley, K.A., 2005,  $^4\text{He}/^3\text{He}$  thermochronometry: Theory, practice, and potential complications: *Reviews in Mineralogy and Geochemistry*, v. 58, p. 181–203, doi:10.2138/rmg.2005.58.7.
- Shuster, D.L., Vasconcelos, P.M., Heim, J.A., and Farley, K.A., 2005, Weathering geochronology by (U-Th)/He dating of goethite: *Geochimica et Cosmochimica Acta*, v. 69, p. 659–673, doi:10.1016/j.gca.2004.07.028.
- Solum, J.G., van der Pluijm, B.A., and Peacor, D.R., 2005, Neocrystallization, fabrics and age of clay minerals from an exposure of the Moab fault, Utah: *Journal of Structural Geology*, v. 27, p. 1563–1576, doi:10.1016/j.jsg.2005.05.002.
- Solum, J.G., Davatzes, N.C., and Lockner, D.A., 2010, Fault-related clay authigenesis along the Moab fault: Implications for calculations of fault rock composition and mechanical and hydrologic fault zone properties: *Journal of Structural Geology*, v. 32, p. 1899–1911, doi:10.1016/j.jsg.2010.07.009.
- Squyres, S.W., and Knoll, A.H., 2005, Sedimentary rocks at Meridiani Planum: Origin, diagenesis, and implications for life on Mars: *Earth and Planetary Science Letters*, v. 240, p. 1–10, doi:10.1016/j.epsl.2005.09.038.
- Steph, S., 2005, Pliocene Stratigraphy and the Impact of Panama Uplift on Changes in Caribbean and Tropical East Pacific Upper Ocean Stratification (6–2.5 Ma) [Ph.D. thesis]: Kiel, Germany, Universität Kiel, 158 p.
- Tremblay, M.M., Shuster, D.L., and Balco, G., 2014a, Diffusion kinetics of  $^3\text{He}$  and  $^{21}\text{Ne}$  in quartz and implications for cosmogenic noble gas paleothermometry: *Geochimica et Cosmochimica Acta*, v. 142, p. 186–204, doi:10.1016/j.gca.2014.08.010.
- Tremblay, M.M., Shuster, D.L., and Balco, G., 2014b, Cosmogenic noble gas paleothermometry: Earth and Planetary Science Letters, v. 400, p. 195–205, doi:10.1016/j.epsl.2014.05.040.
- Trudgill, B.D., 2011, Evolution of salt structures in the northern Paradox Basin: Controls on evaporite deposition, salt wall growth and supra-salt stratigraphic architecture: *Basin Research*, v. 23, p. 208–238, doi:10.1111/j.1365-2117.2010.00478.x.
- Vasconcelos, P.M., 1999, K-Ar and  $^{40}\text{Ar}/^{39}\text{Ar}$  geochronology of weathering processes: *Annual Review of Earth and Planetary Sciences*, v. 27, no. 1, p. 183–229, doi:10.1146/annurev.earth.27.1.183.
- Vasconcelos, P.M., Becker, T.A., Renne, P.R., and Brimhall, G.H., 1992, Age and duration of weathering by  $^{40}\text{K}$ - $^{39}\text{Ar}$  and  $^{40}\text{Ar}/^{39}\text{Ar}$  analysis of potassium-manganese oxides: *Science*, v. 258, p. 451–455, doi:10.1126/science.258.5081.451.
- Vasconcelos, P.M., Renne, P.R., Brimhall, G.H., and Becker, T.A., 1994, Direct dating of weathering phenomena by K-Ar analysis of supergene K-Mn oxides: *Geochimica et Cosmochimica Acta*, v. 58, p. 1635–1665, doi:10.1016/0016-7037(94)90565-7.
- Vasconcelos, P.M., Heim, J.A., Farley, K.A., Monteiro, H., and Waltenberg, K., 2013,  $^{40}\text{Ar}/^{39}\text{Ar}$  and (U-Th)/He- $^4\text{He}/^3\text{He}$  geochronology of landscape evolution and channel iron deposit genesis at Lynn Peak, Western Australia: *Geochimica et Cosmochimica Acta*, v. 117, p. 283–312, doi:10.1016/j.gca.2013.03.037.
- Waltenberg, K.M., 2012, Mineral physics and crystal chemistry of minerals suitable for weathering geochronology: Implications to  $^{40}\text{Ar}/^{39}\text{Ar}$  and (U-Th)/He geochronology [PhD. thesis]: University of Queensland, 421 p.
- Waltenberg, K., Vasconcelos, P.M., and Thiede, D., 2010, Argon diffusivity in 2x2 (hollandite), 2x3 (romanéchite), and 3x3 (todorokite) tunnel manganese oxides: San Francisco, California, American Geophysical Union, Fall Meeting supplement, Abstract V51A-2168, 13–17 December.
- Weber, K.A., Spanbauer, T.A., Wacey, D., Kilburn, M.R., Loope, D.B., and Kettler, R.M., 2012, Biosignatures link microorganisms to iron mineralization in a paleo-aquifer: *Geology*, v. 40, p. 747–750, doi:10.1130/G33062.1.
- Wernicke, R.S., and Lippolt, H.J., 1993, Botryoidal hematite from the Schwarzwald (Germany): Heterogeneous uranium distributions and their bearing on the helium dating method: *Earth and Planetary Science Letters*, v. 114, p. 287–300, doi:10.1016/0012-821X(93)90031-4.
- Wernicke, R.S., and Lippolt, H.J., 1994a,  $^4\text{He}$  age discordance and release behavior of a double shell botryoidal hematite from the Schwarzwald, Germany: *Geochimica et Cosmochimica Acta*, v. 58, no. 1, p. 421–429, doi:10.1016/0016-7037(94)90474-X.
- Wernicke, R.S., and Lippolt, H.J., 1994b, Dating of vein specularite using internal (U+Th)/He isochrons: *Geophysical Research Letters*, v. 21, no. 5, p. 345–347, doi:10.1029/94GL00014.
- White, W.B., Vito, C., and Scheetz, B.E., 2009, The mineralogy and trace element chemistry of black manganese oxide deposits from caves: *Journal of Caves and Karst Studies*, v. 71, no. 2, p. 136–143.
- Wigley, M., Kampman, N., Dubacq, B., and Bickle, M., 2012, Fluid-mineral reactions and trace metal mobilization in an exhumed natural  $\text{CO}_2$  reservoir, Green River, Utah: *Geology*, v. 40, p. 555–558, doi:10.1130/G32946.1.
- Wilson, J.H., McLennan, S.M., Glotch, T.D., Rasbury, E.T., Gierlowski-Kordesch, E.H., and Tappero, R.V., 2012, Pedogenic hematitic concretions from the Triassic New Haven Arkose, Connecticut: Implications for understanding Martian diagenetic processes: *Chemical Geology*, v. 312–313, p. 195–208, doi:10.1016/j.chemgeo.2012.04.013.
- Wolf, R.A., Farley, K.A., and Kass, D.M., 1998, Modeling of the temperature sensitivity of the apatite (U-Th)/He thermochronometer: *Chemical Geology*, v. 148, no. 1–2, p. 105–114, doi:10.1016/S0009-2541(98)00024-2.
- Zhang, X., Prange, M., Steph, S., Butzin, M., Krebs, U., Lunt, D.J., Nisancioglu, K.H., Park, W., Schmittner, A., Schneider, B., and Schulz, M., 2012, Changes in equatorial Pacific thermocline depth in response to Panamanian seaway closure: Insights from a multi-model study: *Earth and Planetary Science Letters*, v. 317–318, p. 76–84, doi:10.1016/j.epsl.2011.11.028.

SCIENCE EDITOR: BRADLEY S. SINGER  
ASSOCIATE EDITOR: J. BRUCE H. SHYU

MANUSCRIPT RECEIVED 30 JULY 2016  
REVISED MANUSCRIPT RECEIVED 2 MAY 2017  
MANUSCRIPT ACCEPTED 17 JUNE 2017

Printed in the USA